Co-funded by the European Union

Research Fund for Coal & Steel

# Hybrid energy storage system using post-mining infrastructure (HESS)

HESS

Deliverable 5.2.

*TES performance report*

**31.12.2025**

| PROJECT | |
|---|---|
| Project number | 101112380 |
| Project name | Hybrid energy storage system using post-mining infrastructure |
| Project acronym: | HESS |
| Call | RFCS-2022 |
| Topic | RFCS-01-2022-RPJ |
| Type of action | RFCS-PJG |
| Service | REA/B/01 |

## DOCUMENT PROPERTIES

| Document Number | D.5.2. |
|---|---|
| Document Title | TES performance report |
| Document responsible | SUT |
| Target dissemination level | PU |
| Document authors | Jakub Ochmann (SUT)<br>Krzysztof Rusin (SUT)<br>Łukasz Bartela (SUT)<br>Tomasz Spietz (ITPE)<br>Kinga Kulik (ITPE)<br>Szymon Dobras (ITPE)<br>Agata Czardybon (ITPE) |
| Date of the document | 31.12.2025 |

Co-funded by the European Union
Research Fund for Coal & Steel

## Table of contents

# 1. Introduction

The integration of Renewable Energy Sources (RES) with national energy systems poses many challenges. One of them is the flexibility of the dispatchable power sources to adjust power generation to the load and current output from RES. One way to tackle this problem is to integrate energy storage into larger systems [1], e.g. power units [2], [3], [4]. This enables the storage of surplus energy from the generating unit as heat when demand can be satisfied by RES generation, and its release when power shortages occur. A crucial part of such a system is Thermal Energy Storage (TES).

Thermal Energy Storage is a large, thick-walled tank filled with a suitable accumulating material. The operation of TES consists of three stages: charging, storage, and discharging. Charging is triggered when surplus energy is available on the energy market. In the context of adiabatic compressed air energy systems (A-CAES), the heat for storage comes from the compression process. The working medium transfers heat to the TES bed and, after being cooled, is stored under high pressure. The storage stage occurs before the projected peak demand. The discharging stage is triggered when the demand for electricity or heat is high, and the energy system requires additional supply from storage. In such a case, pressurised working medium flows through the TES bed and absorbs heat, increasing its enthalpy. Electric power is generated in a turbine where the working medium expands.

Apart from being a component of integrated systems, TES can also operate as a standalone unit [5], [6] and supply heat to end-users [7]. Heat in TES is stored in the form of sensible or latent heat [8]. In the former case, the heat transfer to the bed causes an increase in the bed temperature; in the latter case, the accumulating material, which can be either solid [9], [10] or liquid, changes phase [11], [12].

TES systems using liquids are generally single- or double-tank structures. In the single tank structure, the thermocline phenomenon is utilized [13]. In such a case, the low-density hot medium is driven by buoyancy towards the top of the storage; therefore, high thermal potential is maintained due to thermal stratification. In double-tank structures, hot and cold media are separated to avoid mixing and exergy losses. However, such a design is more technically complicated.

For solid accumulating materials, diaphragm or non-diaphragm TES tanks are used. The working medium is in direct contact with the filling in non-diaphragm tanks, ensuring uniform heat distribution. However, high pressure losses may occur due to flow resistance. This problem can be mitigated in a diaphragm tank, where the bed filling is separated from the heat transfer fluid. However, heat transfer is not as intense as in non-diaphragm tanks, which results in a temperature decrease with the distance from the diaphragm and therefore lower thermal potential during the discharging stage.

Selecting the bed filling material poses a major challenge. On the one hand, the physical properties of the bed must be suitable for a given temperature range, heat transfer fluid and working conditions of the TES tank. These properties should also remain stable over many operating cycles, and the material must not decompose. On the other hand, the material cost should not undermine the economic feasibility of the system. The most frequently used materials are basalt, granite and ceramics [14], [15]. These materials can operate at high temperatures (above 300 °C) and are relatively inexpensive. Apart from the physical properties, the geometry and size distribution of the rocks play a major role in heat transfer. Small pebbles allow for a high contact area between the bed and heat transfer fluid, but at the expense of much higher pressure losses. On the other hand, larger sizes of the rocks reduce pressure losses in the tank, but can lead to higher thermal outlet losses.

Another group of storage materials that were thoroughly analyzed for potential use in TES as part of the HESS project are phase change materials (PCMs), which store heat in the form of latent heat of fusion. Phase change materials (PCMs) store energy primarily through latent heat of phase change, allowing for significantly greater energy storage at a nearly constant temperature. As a result, TES based on PCMs should exhibit higher energy density, a stable temperature profile during charge and discharge, and greater efficiency with less space occupied by the system. However, PCMs require encapsulation to prevent leakage during melting, and their thermal conductivity is lower than that of rock materials, which can limit the heat transfer rate. Additional challenges include long-term stability issues e.g., phase segregation or cyclic degradation as well as higher material cost.

Thermal Energy Storage may appear to be a relatively simple part of energy systems, but complex physical phenomena and multiple operating parameters that must be specified, together with physical properties of accumulating materials, make the correct design a challenging task.

# 2. Aim of the work

The objective of this report is to present experimental investigations of heat transfer and thermal energy storage processes using storage units based on both single-phase materials and phase-change materials as heat-accumulating media. Within the framework of the *Hybrid Energy Storage System Using Post-Mining Infrastructure* project, the application of thermal energy storage units is envisaged to fulfill a number of functions. For example, from the perspective of an adiabatic compressed air energy storage system, efficient thermal energy storage is a key factor in eliminating the need for fuel combustion (e.g., natural gas) during the discharge stage.

The experimental results presented also served as a basis for the validation of the developed numerical models of the thermal energy storage units. These validated models enabled the execution of multi-variant analyses, constituting a preliminary stage for further research on the proposed energy storage systems.

# 3. Methodology

## 3.1. Experimental stand (Silesian University of Technology)

The first phase of the experimental investigation of the thermal energy storage system was carried out on a laboratory test stand, the key component of which was a heat storage unit with a volume of approximately 0.1 m3. The geometry of the storage unit was characterized by a notably high slenderness ratio compared to previously investigated configurations; the height of the unit was 3 m, while its internal diameter was 0.213 m [16]. This design resulted from the concept of developing a thermal energy storage unit for application in an adiabatic compressed air energy storage system [9].

The test stand was designed and constructed by the research team from the Department of Power Engineering and Turbomachinery at the Silesian University of Technology and is located in the Hydraulic Machinery Hall building of the Faculty of Energy and Environmental Engineering. The test stand is presented in the photos below [16].

**Figure 1** Thermal Energy Storage tank with a Porous Bed at Silesian University of Technology.

(a) (b)

Figure 2 Components of the experimental setup: (a) air blower with control system; (b) result visualization system.

(a) (b)

Figure 3 Components of the experimental setup: (a) steel pipelines with valves; (b) measurement instruments.

**Figure 4** Thermal storage bed.

In Figures 1 – 4, the main components of the setup are presented, which include [17]:

- 1 – A SC40A 750T side-channel blower equipped with a three-phase electric motor rated at 7.5 kW, supplied by Venture Industries Sp. z o.o. [18], was used. The nominal rotational speed of the blower is 2885 rpm, and speed control is achieved using an SMVector Lenze frequency inverter [19]. The blower is employed to force the airflow serving as the heat transfer medium during both the charging and discharging stages; the maximum air volumetric flow rate is 650 $m^3$/h, and the maximum overpressure is 39,500 Pa;
- 2 – An Aplisens slit-type flow nozzle made of AISI 304 acid-resistant stainless steel, with a nominal diameter of DN80 and a maximum operating pressure of 16 bar, was used. The nominal air mass flow rate is 0.064 kg/s [20];
- 3 – A Leister LE 10000 electric air heater with a rated power of 17 kW was applied. The minimum air flow rate ensuring safe operation of the heater is 78 $m^3$/h, and the maximum allowable inlet overpressure is 100 kPa. The device is capable of heating the flowing gas to a maximum temperature of 650 °C; however, this capability was not fully utilized during the conducted experiments [21];
- 4 – A system of Victaulic Vic-300 MasterSeal butterfly valves, with an applicable operating temperature range of the flowing medium from −34 °C to 110 °C, was used to control the direction of airflow through the thermal energy storage unit [22];
- 5 – A vertical thermal energy storage unit was constructed from stainless steel pipe with a nominal diameter of DN200. The unit was equipped with flat steel flanges enabling to be connected to the inlet and outlet chambers. During the experiments, the thermal energy storage unit was filled with a porous bed formed from basalt rocks.

The temperature of the heat storage material was measured using ten class A PT100 resistance temperature detectors located along the axis of the storage unit [23]. Table 1 defines the measurement errors adopted for calculating the maximum measurement uncertainty associated with the use of class A PT100 temperature sensors [17].

**Table 1** Identified errors and maximum uncertainty of temperature measurement.

| Error classification | Value |
|---|---|
| Temperature error | ±0,15°C + 0,002·T* |
| Signal processing error | ±0,5°C |
| Measurement resolution | ±0,1°C |
| Maximum measurement uncertainty | ±0,36°C |

*°C

One of the key operational parameters of a system employing a thermal energy storage unit with a porous filling is the pressure drop of the gas flowing through the porous bed. This parameter was measured using an Aplisens PR-28 differential pressure transducer with a measuring range of 0 – 10 kPa. According to the device datasheet, the maximum allowable temperature of the measured medium is 120 °C [20]; this limit was not exceeded during the experiments. Table 2 presents the identified measurement errors and the maximum uncertainty of the air pressure drop measurement [17].

**Table 2** Identified errors and maximum uncertainty of air pressure drop measurement.

| Error classification | Value |
|---|---|
| Basic error | ±0,4% |
| Temperature error | ±0,4% / 10°C |
| Error due to supply voltage variations | ±0,005% / 1 V |
| Hysteresis and repeatability | ±0,05% |
| Maximum measurement uncertainty | ±209 Pa |

During the experimental phase, basalt stones with a density of 2680 kg/m³ and a thermal conductivity of approximately 2.3 W/(m·K) were used. The specific heat capacity was adopted based on a previous literature review conducted within the HESS project, and its value is calculated using the following correlation [24]:

$$cp_b = 91.523 \cdot \ln(T_b) + 498.25 \tag{1}$$

where $T_b$ is the temperature of the basalt (°C).

## 3.2. Experimental stand (Institute of Energy and Fuel Processing Technology)

As part of WP5 of the HESS project, the Institute of Energy and Fuel Processing Technology designed and constructed a test rig for investigating heat storage materials in a solid bed. The main component of the installation is a steel column (Thermal Energy Storage unit – TES unit), 1 m in length with an internal diameter of 219 mm, allowing the placement of approximately 30 dm³ of heat storage material. In this test rig, a basalt and a phase-change material (PCM), contained in aluminum containers, were tested. A schematic of the installation is shown in Figure 5.

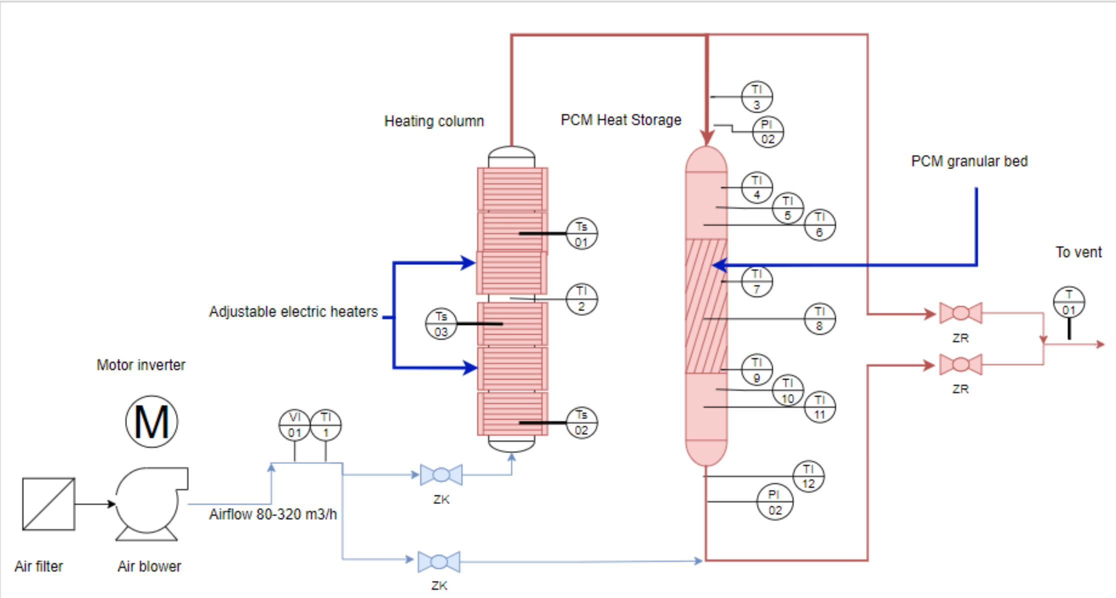


**Figure 5** Diagram of the experimental thermal energy storage installation.

Heat is supplied by an air stream heated in a heating column, consisting of a steel pipe equipped with band heaters with a total power of 15 kW. To enhance the heat transfer surface, the heating column is filled with ceramic balls (Al2O3). The air, with a controllable flow rate, passes through the heating column and is then directed into the column filled with the thermal energy storage (TES) material.

During the charging stage, the heated air flows through the TES column from top to bottom. During the discharging stage, by adjusting the valve settings, cool air is directed in the opposite direction (from bottom to top), extracting the stored thermal energy. The TES column has a bed height of 70 cm and a diameter of 215 mm, with the total column height being 1 m. The TES column is insulated with high-temperature quartz wool (100 mm thick) and high-temperature mineral wool (100 mm thick). This double insulation significantly reduces heat losses and ensures stable measurement conditions.

The installation is fully instrumented, with particular emphasis on temperature measurements at different heights and across the cross-section of the bed. In total, seven thermocouples are embedded within the TES material. For the PCM tests, two thermocouples were placed inside the PCM capsules. Measurement data, including temperatures and air flow, are continuously monitored and recorded. Measurement ports allow for the assessment of pressure and flow resistance. The test rig is designed to operate at temperature up to 500 °C.

(a)

(b)

(c)

**Figure 6** (a) Experimental thermal energy storage setup; (b) heat storage material: basalt; (c) PCM capsules.

The TES charging procedure was conducted as follows:

- The heating column controller was set to the target temperature to heat the air to the planned test temperature. The temperature at the heaters was higher than the target bed temperature due to heat losses in the uninsulated heating column and limitations in heat transfer between the gas and the column. This set temperature was determined experimentally based on preliminary heating tests.
- The air blower controller was then set to the desired flow rate. The air was directed through the heating column into the TES bed.
- The bed was gradually heated until the desired initial temperature was reached. Steady-state conditions were considered achieved when the temperature profiles within the column reached a plateau (i.e., no significant temperature increase over the next 10 minutes). Special attention was given to heating the lower part of the bed, which, due to the top-to-bottom flow of hot air, was heated last. Despite heating and stabilization, a temperature difference of approximately 10 °C between the bottom and top of the bed remained.

It should be noted that during the heating, a minor adjustment of the air flow was necessary to maintain the target value, as the air viscosity increased at elevated temperatures, resulting in higher flow resistance.

The TES discharging procedure was conducted as follows:

- By adjusting the valves, a stream of cool air (bypassing the heating column) was directed through the TES column from bottom to top.
- The airflow rate was set to the specified value for the discharging test. The test continued until the entire bed cooled to approximately 30 – 40 °C.

## 3.3. Evaluation of experimental results

Based on the archived temperature and airflow measurement data, the energy storage parameters were determined.
The total energy supplied to the storage unit during the bed charging process, $Q_{in}$, was calculated as the sum of the energy increments over successive time steps [17]:

$$Q_{in} = \sum_{i=1}^{N} m_{air} C_{p\,air} (T_{in} - T_{out}) \Delta t_i \tag{2}$$

Where $m_{air}$ is the air mass flow rate at time step $i$, $C_{p\,air}$ is the specific heat of air at the mean temperature between $T_{in}$ and $T_{out}$, $T_{in}$ and $T_{out}$ are the inlet and outlet air temperatures of the storage unit at time step i (°C), and $\Delta t_i$ is the time interval between measurements (s).
The energy extracted during the discharging of the storage unit, $Q_{out}$, is calculated analogously to the charging process:

$$Q_{out} = \sum_{i=1}^{N} m_{air} C_{p\,air} (T_{out} - T_{in}) \Delta t_i \qquad (3)$$

The average thermal power (heat output rate), $P_{av}$, during the discharging of the storage unit was calculated based on:

$$P_{av} = \frac{Q_{out}}{t_{disch}} \qquad (4)$$

Where $t_{disch}$ is the total discharging time of the energy storage unit. The energy efficiency of the TES charging/discharging cycle was defined as:

$$\eta_{en} = \frac{Q_{out}}{Q_{in}}$$

The exergy efficiency of the TES cycle was calculated based on methodology presented in [25].

According to the adopted nomenclature, the volume of the storage material bounded by two measurement points is defined as a segment of the storage bed. One of the defined parameters used to evaluate the experimental series was the dimensionless state of charge of the thermal energy storage unit, $\theta_{TES}$, which for a single segment $i$ is expressed as shown in Equation (5):

$$\theta_{TES\,i} = \frac{T_{i\,t} - T_{\min i}}{T_{a\,max} - T_{\min i}}, \qquad (5)$$

where $T_{i\,t}$ and $T_{\min i}$ are, respectively, the temperature of segment $i$ at a given time $t$ and the minimum temperature of the storage material in that segment at the beginning of the charging stage, and $T_{a\,max}$ is the maximum inlet air temperature to the storage unit during the analyzed measurement series. The segment temperature was assumed to be the average of the readings from the adjacent resistance temperature detectors bounding the segment volume. Finally, the value of $\theta_{TES}$ is obtained according to Equation (6):

$$\theta_{TES} = \frac{\theta_{TES\,1} + \theta_{TES\,2} + \cdots + \theta_{TES\,n}}{n} = \frac{\sum_{j=1}^{n} \theta_j}{n}, \qquad (6)$$

where $n$ is the number of segments in the thermal energy storage unit.

For the purpose of evaluating the measurement results, dimensionless parameters were used, whose definitions are presented below:

- The dimensionless inlet air temperature to the thermal energy storage unit during the charging stage, $T_{in\,c}$, is defined as:

$$T_{in\,c} = \frac{T_{in\,a\,c} - T_{a\,min}}{T_{a\,max} - T_{a\,min}}, \qquad (7)$$

where $T_{a\,min}$ is the minimum air temperature during the measurement series, equal to the ambient temperature, and $T_{in\,a\,c}$ is the current inlet air temperature to the TES unit.

- The dimensionless outlet air temperature from the thermal energy storage unit during the discharging stage, $T_{out\ d}$, is defined as:

$$T_{out\ d} = \frac{T_{out\ a\ d} - T_{a\ min}}{T_{a\ max} - T_{a\ min}}, \tag{8}$$

where $T_{out\ a\ d}$ is the current outlet air temperature from the TES unit.

- The dimensionless temperature of the rock material at a given point, $T_{R\ s}$, is defined as:

$$T_{R\ s} = \frac{T_s - T_{s\ min}}{T_{a\ max} - T_{s\ min}}, \tag{9}$$

where $T_{s\ min}$ is the minimum temperature of the rock material at the given point, and $T_s$ is the current temperature of the rock material at that point.

- The dimensionless time of the charging stage,$\tau_{R\ c}$, is defined as:

$$\tau_{R\ c} = \frac{t_c}{t_{c\ max}}, \tag{10}$$

where $t_{c\ max}$ is the maximum duration of the TES charging stage, and $t_c$ is the current time elapsed during the charging stage.

- The dimensionless time of the discharging stage, $\tau_{R\ d}$, is defined as:

$$\tau_{R\ d} = \frac{t_d}{t_{d\ max}}, \tag{11}$$

where $t_{d\ max}$ is the maximum duration of the TES discharging stage, and $t_d$ is the current time elapsed during the discharging stage.

For the evaluation of the performance of the thermal energy storage unit with a storage bed, an outlet loss parameter, $T_o$, during the charging stage was also defined. This parameter relates the outlet air temperature, $T_{out\ c}$, to the characteristic temperatures of the given measurement series, namely $T_{a\ min}$ and $T_{a\ max}$, according to Equation (12):

$$T_o = \frac{T_{out\ c} - T_{a\ min}}{T_{a\ max} - T_{a\ min}}. \tag{12}$$

## 3.4. Numerical Model – Sensible Heat Storage Unit

The modeling of the rock bed region was performed using the porous zone model in ANSYS Fluent, which incorporates momentum source terms accounting for viscous and inertial resistance, as well as the effect of porosity on the flow. The momentum conservation equation for the applied model is as follows:

$$\varepsilon\rho_f\left(\frac{\partial\vec{v}}{\partial t}+\vec{v}\cdot\nabla\vec{v}\right)$$
$$=-\varepsilon\nabla p+\nabla\cdot\left(\mu_{eff}\cdot\left(\nabla\vec{v}+(\nabla\vec{v})^T\right)\right)-\left(\frac{\mu}{\alpha}+\frac{C_2\rho_f}{2}|\vec{v}|\right)\vec{v}+\varepsilon\vec{F}, \quad (13)$$

where $\varepsilon$ is the bed porosity, $\rho_f$ is the fluid density, $\vec{v}$ is the velocity vector, $p$ is the pressure, $\mu$ is the dynamic viscosity of the fluid, $\mu_{eff}$ is the effective viscosity including turbulent effects, $\vec{F}$ represents other external forces, and $\alpha$is the permeability of the porous medium, defined as:

$$\alpha=\frac{{D_p}^2}{150}\cdot\frac{\varepsilon^3}{(1-\varepsilon)^2}. \quad (14)$$

The inertial resistance coefficient, $C_2$, is defined as:

$$C_2=\frac{3{,}5}{D_p}\cdot\frac{(1-\varepsilon)}{\varepsilon^3}. \quad (15)$$

The correlation for the porosity distribution of the rock bed, which was also used in the numerical studies by Cascetta et al. [26], is presented in Equation (16):

$$\varepsilon(y)=\left(1+\left(\frac{1-\varepsilon_\infty}{\varepsilon_\infty}\right)\cdot\left(1-e^{-2y}\right)^{1/2}\right)^{-1}, \quad (16)$$

The heat transfer between the fluid and the rock material was implemented using the Local Thermal Non-Equilibrium (LTNE) model [27]. This approach duplicates the porous zone of the geometric model and allows for the appropriate assignment of material properties to the air and the storage material. The LTNE model introduces an energy conservation equation for each of the defined regions. The energy conservation equation for the fluid zone is defined in Equation (17), while for the storage material zone it is defined in Equation (18):

$$\varepsilon\rho_f cp_f\left(\frac{\partial T_f}{\partial t}+\vec{v}\cdot\nabla T_f\right)=\nabla\cdot\left(\varepsilon k_{eff}\nabla T_f\right)+h_{fs}A_{fs}(T_s-T_f), \quad (17)$$

$$(1-\varepsilon)\rho_s cp_s\frac{\partial T_s}{\partial t}=\nabla\cdot\left((1-\varepsilon)k_{eff}\nabla T_s\right)+h_{fs}A_{fs}\left(T_f-T_s\right), \quad (18)$$

where $c_{p,f}$ and $c_{p,s}$ are the specific heat capacities of the fluid and the solid material, respectively; $T_f$ and $T_s$ are the temperatures of the fluid and the solid material, respectively; $h_{fs}$ is the heat transfer coefficient between the fluid and the solid; and $A_{fs}$ is the heat transfer surface area between the fluid and the solid, defined as:

$$A_{fs} = 6 \cdot \frac{1-\varepsilon}{D_p}. \tag{19}$$

Equation (20) presents the correlation for the Nusselt number in a porous bed used in this study, as proposed by Wakao et al. [28]:

$$Nu = 2 + 1{,}1 \cdot Re^{0{,}6} \cdot Pr^{1/3} = \frac{h_{fs} \cdot D_p}{k_f}, \tag{20}$$

where the Reynolds and Prandtl numbers are defined according to Equations (21) and (22):

$$Re = \frac{v_\infty \cdot D_p}{v_f}, \tag{21}$$

$$Pr = \frac{cp_f \cdot \mu_f}{k_f}, \tag{22}$$

where $\nu_f$ is the kinematic viscosity of the fluid, and $v_\infty$ is the superficial velocity in the porous medium, directly derived from the continuity equation of the flow:

$$v_\infty = \frac{\dot{m}_{htf}}{\rho_f \cdot A_{TES}}, \tag{23}$$

where $\dot{m}_{htf}$ is the mass flow rate of the fluid passing through the porous bed, and $A_{TES}$ is the cross-sectional area of the TES unit.

The effective thermal conductivity within the porous zone, $k_{eff}$, is calculated based on the volumetric fractions of the storage material and air, according to Equation (24):

$$k_{eff} = \varepsilon \cdot k_f + (1-\varepsilon) \cdot k_s, \tag{24}$$

where $k_f$ and $k_s$ are the thermal conductivities of the fluid and the solid material, respectively. The mass conservation equation for the porous zone is defined as:

$$\frac{\partial(\varepsilon\rho_f)}{\partial t} + \nabla \cdot (\varepsilon\rho_f \vec{v}) = 0. \tag{25}$$

During the calculations, the k–ω SST turbulence model was used, which is a combination of the k–ω and k–ε models, providing accurate flow simulation across the entire computational domain [29], [30]. This model employs two additional transport equations – one for the turbulent kinetic energy, $k$ (presented in Equation (26)), and one for the specific dissipation rate of turbulence, $\omega$ (presented in Equation (27)) – to determine the turbulent viscosity:

$$\varepsilon\rho_f \frac{\partial k}{\partial t} + \varepsilon p \vec{v} \cdot \nabla k = \nabla \cdot \left( \left( \mu + \frac{\mu_t}{\sigma_k} \right) \nabla k \right) + P_k - \varepsilon\rho_f \beta^* k\omega, \tag{26}$$

$$\begin{aligned}\varepsilon\rho_f\frac{\partial\omega}{\partial t}+\varepsilon p\vec{v}\cdot\nabla\omega \\ &=\nabla\cdot\left(\left(\mu+\frac{\mu_t}{\sigma_\omega}\right)\nabla\omega\right)+\gamma\frac{\omega}{k}P_k-\varepsilon\rho_f\beta\omega^2 \\ &+(1-F_1)\frac{2p\sigma_{\omega 2}}{\omega}\nabla k\cdot\nabla\omega,\end{aligned} \tag{27}$$

where $\beta^*$, $\beta$, and $\gamma$are constants for the SST model, $\sigma_k$ and $\sigma_\omega$ are the diffusion coefficients for $k$ and $\omega$, respectively, and $F_1$is the so-called blending function, which enables a stable transition between the k–ω and k–ε models depending on the proximity of the flow to the wall.

## 3.5. Numerical Model – Latent Heat Storage Unit

In Ansys Fluent, the solver solves systems of partial differential equations that are related to the conservation of mass, momentum and energy in flows. Integrating the equations in the control volume leads to their discretisation, i.e. the transformation of continuous equations (in the differential sense) into systems of algebraic equations. The systems of partial differential equations were solved simultaneously using a partially hidden iterative algorithm (SIMPLE). The pressure distribution option (PRESTO!) was adopted for the pressure correction equation, and second-order upwind schemes were used to solve the momentum and energy equations. Underelaxation factors were used for the calculations, with a value of 0.7 for solving the momentum equation, 0.3 for the pressure correction equation, 1 for the energy equation, and 0.1 for the liquid fraction equation.  The equations of conservation of mass and momentum are taken into account for all flows. In the case of heat transport, the equation of conservation of energy is also added. The equation of conservation of mass has the form [31].

$$\frac{\partial\rho}{\partial t}+\nabla(\rho\vec{v})=S_m \tag{28}$$

where: $S_m$ is part responsible for mass sources added to the continuous phase from the (dispersed) phase, e.g. as a result of evaporation of liquid droplets and any user-defined mass sources

The momentum conservation equation is expressed as [31]:

$$\frac{\partial}{\partial t}(\rho\vec{v})+\nabla(\rho\vec{v}\vec{v})=-\nabla\mathrm{p}+\nabla\bar{\bar{\tau}}+p\vec{g}+\vec{F} \tag{29}$$

Where p is static pressure, $p\vec{g}$ is gravitational force and $\vec{F}$ is term responsible for external forces acting on the body, e.g. as a result of interaction with the dispersed phase, as well as for other source factors depending on the model used. The calculations used a laminar flow model, which is described by the unsteady Navier-Stokes equations. This model is suitable for situations where the fluid flow is stable, orderly and does not exhibit turbulent characteristics. Laminar flow is characterised by fluid particles moving in smooth, parallel layers without mixing. The choice of flow model is determined by the Reynolds number (Re), which is a measure of the ratio of inertial forces to viscous forces in fluid flow. For low Reynolds numbers (Re<2000), the flow is laminar and turbulence is not a significant phenomenon, as the viscous forces are strong enough to prevent irregular movement of fluid molecules. The Reynolds number is expressed by the formula [31]:

$$Re = \frac{wl_0}{v} \tag{30}$$

Where $w$ is characteristic flow velocity (m/s), respectively $l_0$ is characteristic dimension (m) and $v$ is kinematic viscosity of the fluid ($m^2/s$).

The enthalpy of a material is calculated as the sum of the sensible enthalpy h and the latent heat ΔH [31]:

$$H = h + \Delta H \tag{31}$$

$$h = h_{ref} + \int_{Tref}^{T} c_p dT \tag{32}$$

Where $h_{ref}$ is reference enthalpy, $T_{ref}$ is reference temperature and $c_p$ specific heat at constant pressure.

Liquid fraction β, is defined as [31]:

$$\begin{aligned} &\beta=0 && \text{if} \quad T < T_{solidus} \\ &\beta=1 && \text{if} \quad T > T_{liquidus} \\ &\beta=\frac{T-\mathrm{T}solidus}{\mathrm{T}liquidus-\mathrm{T}solidus} && \text{if} \quad T_{solidus} < T < T_{liquidus} \end{aligned} \tag{33}$$

The amount of latent heat can be expressed in terms of the latent heat of the material, L

$$\Delta H = \beta L \tag{34}$$

The latent heat content can range from zero (for solids) to L (for liquids).

For solidification/melting problems, the energy equation is written as:

$$\frac{\partial}{\partial t}(\rho H) + \nabla(\rho\vec{v}H) = \nabla(\mathrm{k}\nabla\mathrm{T}) + \mathrm{S} \tag{35}$$

Where$H$ is enthalpy, $\rho$ is density, $\vec{v}$ is fluid velocity and S is heat source.

ANSYS Fluent can be used to model solidification and/or melting phenomena occurring at a single temperature or within a temperature range. The transition area between the liquid and the solid is treated as a porous zone in which the porosity corresponds to the liquid fraction. Appropriate momentum absorption terms are introduced into the momentum equations to account for the pressure drop associated with the presence of a solid during the solidification process. In the case of solidification and melting of a pure substance, the phase transition occurs at a specific melting temperature $T_{melt}$. However, in the case of a multicomponent mixture, there is a solidification/melting zone between the lower temperature (solidus) and the upper temperature (liquidus). When a multicomponent liquid solidifies, the dissolved substances transition from the solid phase to the liquid phase. This effect is quantified by the solute partition coefficient, denoted by Ki, which determines the ratio of the mass fraction in the solid to the mass fraction in the liquid at the phase boundary.

The solidification and melting temperatures of a mixture are described as [31]:

$$T_{solidus} = T_{melt} + \sum m_i Y_i / K_i \tag{36}$$

$$T_{liquidus} = T_{melt} + \sum m_i Y_i \tag{37}$$

Where $K_i$ is solute partition coefficient, $Y_i$ is mass fraction of solute, $m_i$ is slope of the liquidus surface to $Y_i$.

Many substances participate in the process of solidification or melting, and the density of liquids varies depending on temperature and composition. In the presence of a gravitational field, buoyancy is caused by two mechanisms: thermal buoyancy refers to the buoyancy force acting on a fluid as a result of density differences caused by temperature changes. Thermal buoyancy promotes liquid mixing and temperature gradient smoothing, and its omission can lead to inaccurate solidification time predictions. Solutal buoyancy results from the gravitational force caused by a change in density due to a change in the species composition of the molten material. Modelling buoyancy effects is important for accurately predicting solidification behaviour. In ANSYS Fluent, buoyancy-induced flows in multiphase solidification problems are modelled using the Boussinesq approach [31]:

$$\vec{F_s} = \rho_{ref} \vec{g} \sum_{i=0}^{N_s} \beta_{s,i} (y_{l,i} - y_{ref,i}) \tag{38}$$

Where $y_{l,i}$ is the mass fraction of the i-th solute in the liquid phase, $y_{ref,i}$ is reference mass fraction of the i-th species $\beta_{s,i}$ is the expansion coefficient of the i-th species, $N_s$ is total number of dissolved substances, $g$ is gravitational constant, $\rho_{ref}$ is reference density.

# 4. Results

## 4.1. Experimental analysis - Sensible heat storage

Figures 7 (a) – 7 (b) show the typical temperature variation of the storage material at 10 measurement points in the experimental test stand operated by the Silesian University of Technology, illustrating the temperature increase during the charging stage of the storage unit and the temperature decrease during the discharging stage.

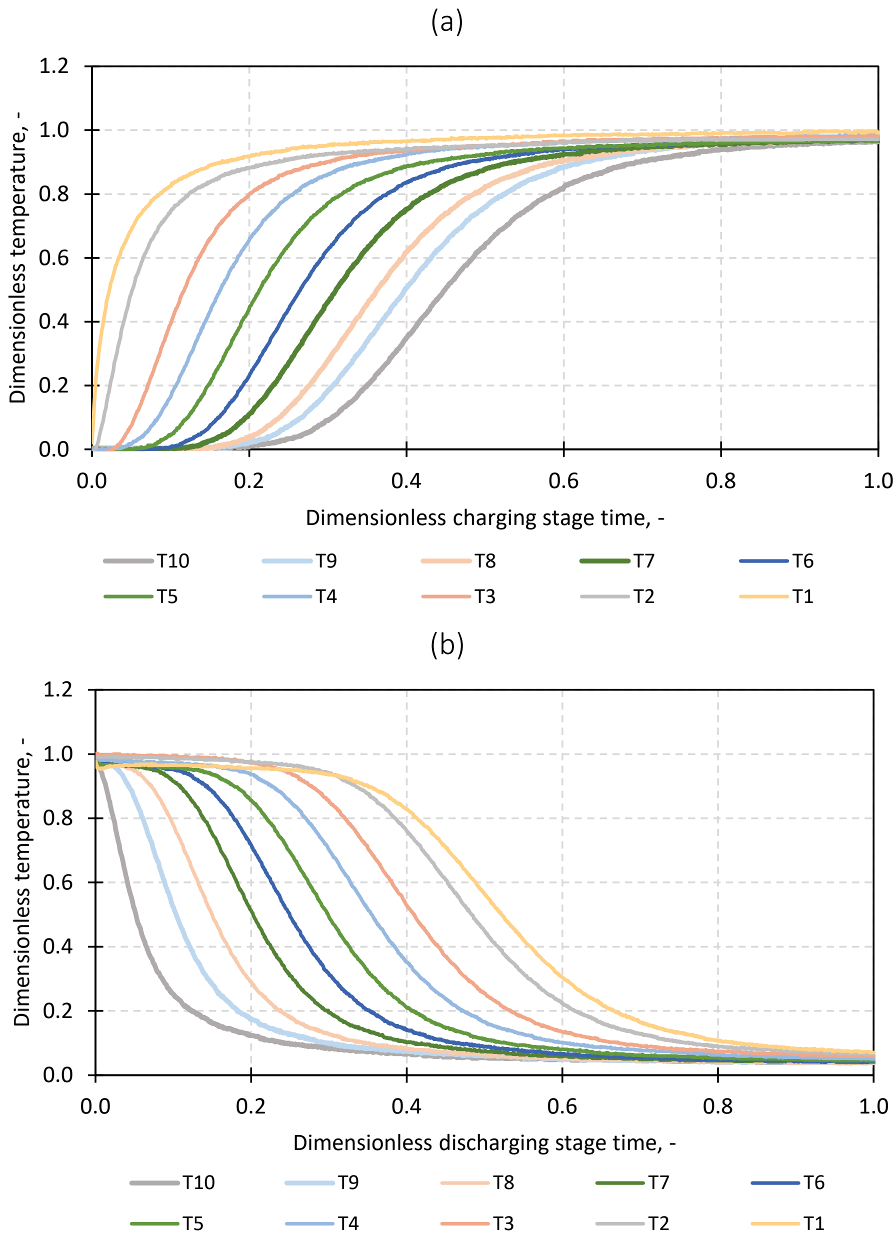


**Figure 7** Variation of the measured temperature at the measurement points: (a) charging stage; (b) discharging stage.

The characteristics presented in Figures 7 (a) – 7 (b) illustrate the key features and operational parameters of the thermal energy storage unit with a porous bed, which can significantly impact the performance of a potential adiabatic compressed air energy storage system analyzed within the HESS project. The identified features are:

- The maximum recorded temperature of the storage material does not reach the maximum setpoint of the inlet air temperature to the storage unit, even under steady-state thermodynamic conditions. This is due to imperfect heat transfer between the air and the storage material, and the maximum basalt temperature will asymptotically approach the maximum air temperature within a given experimental series.
- Heat exchange between the air and the rock material during airflow through the storage unit results in a non-uniform temperature distribution of the storage material, with a decrease toward the outlet.
- During the charging stage, an increase in the outlet air temperature (T10) is observed after a relatively short time. An increase in outlet losses from the storage unit is undesirable from the perspective of full-scale energy storage system operation; therefore, it should be minimized, for example, by increasing the volume of the storage material relative to the amount of heat supplied.
- During the discharging stage, it is not possible to maintain a constant outlet air temperature from the TES unit, which will have a direct impact on the decrease in air expander power in the considered A-CAES system.

Figure 8 presents the experimental characteristics showing the time of onset of outlet losses from the storage unit as a function of air mass flow rate during the charging stage and the particle size of the storage bed used [17].

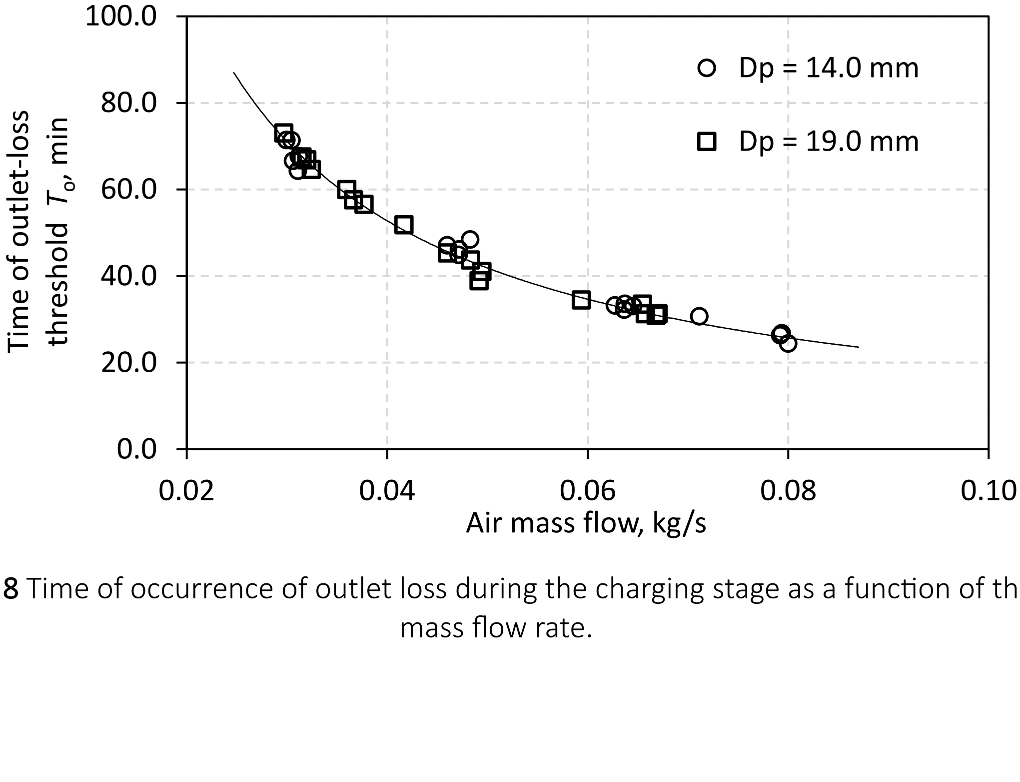


**Figure 8** Time of occurrence of outlet loss during the charging stage as a function of the air mass flow rate.

Based on all conducted experimental series – 34 independent measurement series in total – it was demonstrated that a relationship exists between the time of occurrence of the selected threshold outlet loss and the applied air mass flow rate during the charging of the thermal energy storage unit. As the air mass flow rate decreases, the time to reach the outlet loss extends, which is attributed to the gas velocity through the storage bed and the time required for heat exchange between the phases. For the particle sizes used, no significant effect of this parameter on the time to reach the threshold outlet loss was observed.

From a theoretical perspective, a decrease in mass flow should correspond to an increase in the time $T_0$. The absence of experimental confirmation of this relationship may be due to the relatively small volume of the tested storage bed and differences in particle size of the storage materials.

Figure 9 presents the experimental relationship between the pressure drop of air flowing through the storage bed and the air mass flow rate for two different particle sizes of the investigated storage beds. The presented characteristics were obtained for unheated inlet air, i.e., at ambient temperature.

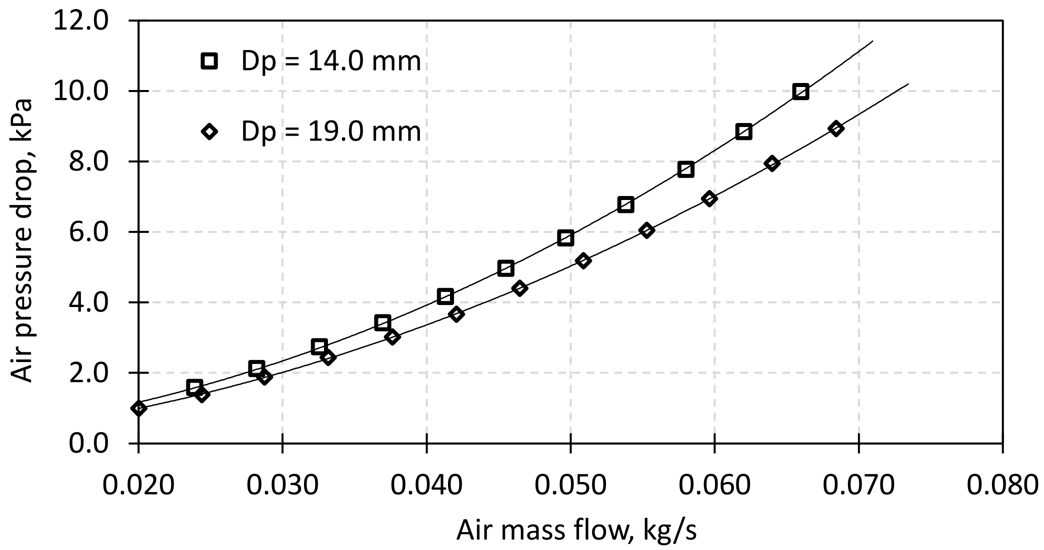


**Figure 9** Air pressure drop as a function of the air mass flow rate.

The pressure drop of air flowing through the thermal energy storage unit is a critical parameter for the operation of a full-scale adiabatic compressed air energy storage system. The level of pressure losses directly affects the power of both the compressor and the air expander. During the WP4 studies, the pressure losses were determined as a function of the storage unit diameter, which influenced the flow velocity for a given air mass flow rate. The experimental investigations confirmed that an increase in air mass flow rate is accompanied by a corresponding increase in pressure drop. The magnitude of the losses is also affected by the particle size of the rock bed used.

Within the experimental studies conducted at ITPE, two types of materials were investigated: basalt, representing a conventional material with high thermal stability for sensible heat storage, and a PCM, known as SolarSalt, characterized by its ability to store large amounts of energy through a phase transition (latent heat) [24]. The basalt grains was delivered to ITPE by Silesian University of Technology (SUT), so they were identical to those tested previously by SUT. TES unit contained approximately 42 kg of basalt, corresponding to a volume of 25 $dm^3$.

Example temperature profiles during the charging of the basalt-filled storage unit are shown in the graphs in Figure 10. The plots depict the temperatures of the inlet gas, outlet gas, and the internal bed at the top, middle, and bottom. Figure 10 a) illustrates the charging of the storage unit to 150 °C, while Figure 10 b) shows charging to 330 °C (average bed temperature). In both cases, the air flow rate was approximately 60 kg/h. It is clearly observed that heating to more than twice the temperature required roughly twice the time – 100 minutes for 150 °C and 200 minutes for 330 °C.

(a)

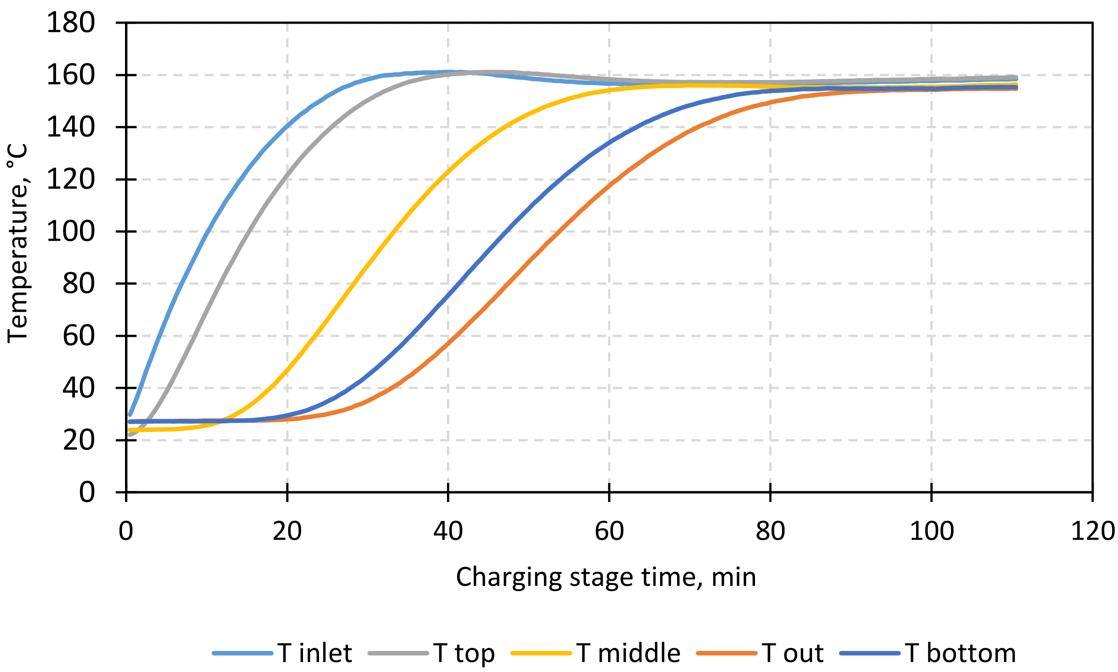

(b)

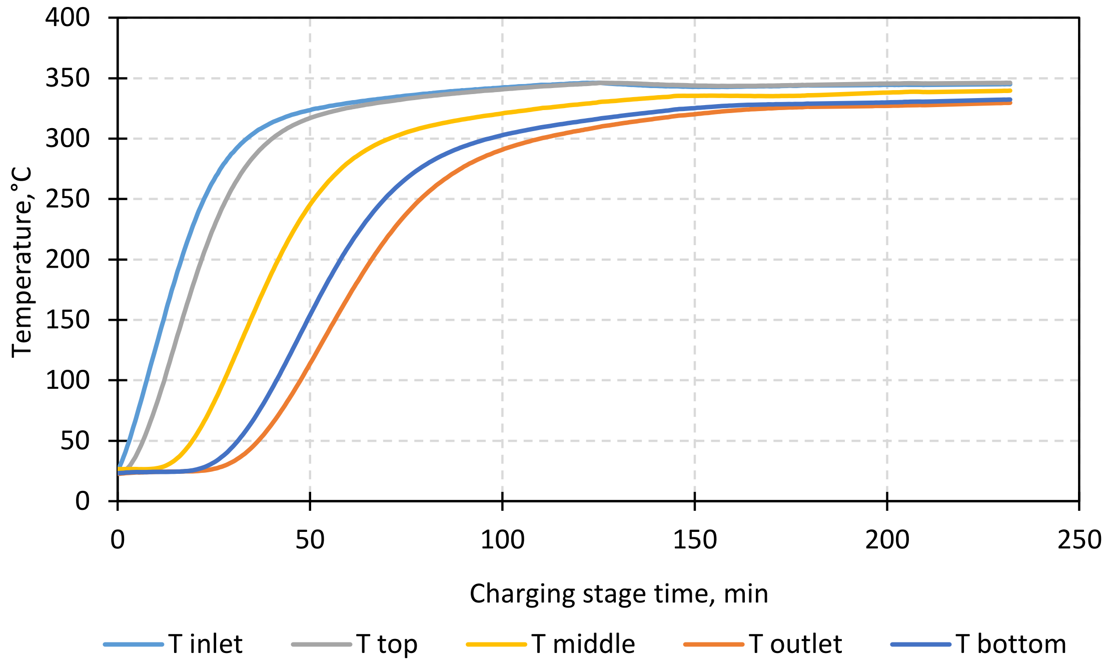


**Figure 10** Charging of the energy storage unit for an air flow rate of 60 kg/h to two target temperatures: (a) 150 °C and (b) 300 °C.

Figure 11 presents the temperature distribution during the charging stage of the storage unit, both along the height of the TES bed and at measurement points located away from the column axis ($T_b$ – bottom, $T_m$ – middle). As observed, the temperature differences at points slightly offset from the axis are small, and in many instances the temperatures nearly coincide with the axial measurements. Maximum deviations reach up to 5 °C, whereas the accuracy of the thermocouples used is ±2 °C. Therefore, the primary source of these deviations is the measurement uncertainty of the thermocouples. The observed distribution indicates good hot air circulation within the column and effective heat transfer.

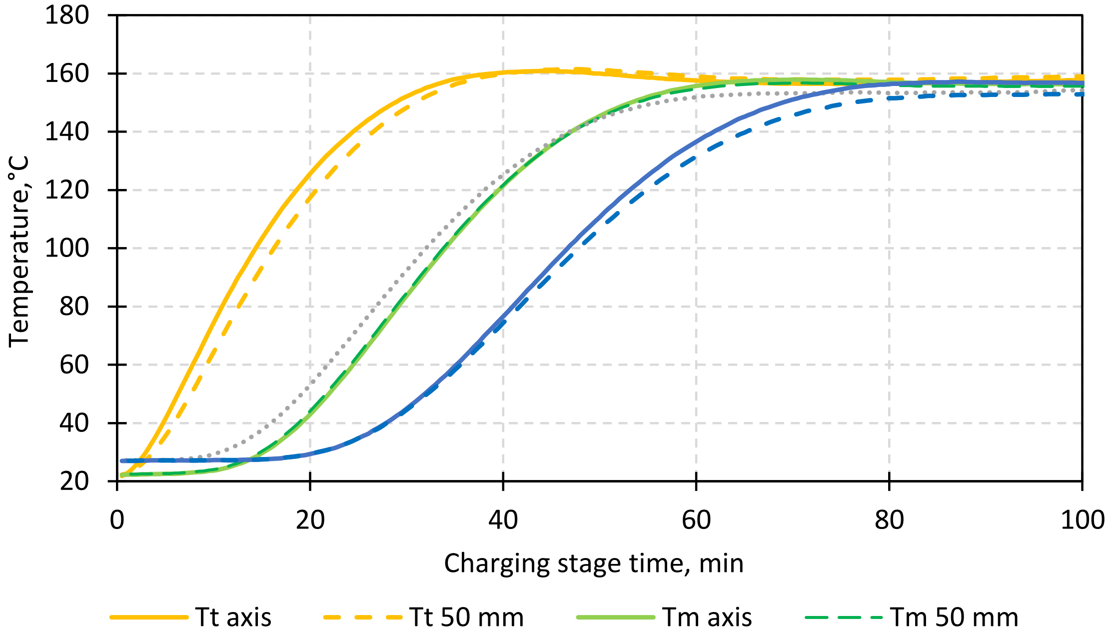


**Figure 11** Temperature distribution in the bed during charging at different points across the TES tank and at various heights.

To compare the heating dynamics of the TES bed at air flows of 60 and 120 kg/h, the temperature distribution along the column axis was compiled into a single graph (

Figure **12**). The curves show the temperatures in the upper (T top), middle (T mid), and lower (T bottom) parts of the bed.

For both mass flow rates, a progressive temperature increase is observed along the column axis, reflecting the propagation of the heating front from the hot air inlet. The fastest temperature response occurs near the inlet (T top), followed by the middle section (T mid), while the lowest heating rate is observed in the region farthest from the heat source (T bottom).

Increasing the air mass flow rate to 120 kg/h significantly increases the heating of the bed, as evidenced by steeper temperature rises during the initial stage and the reduced time delays between measurement zones. As a result, a more uniform temperature distribution is established at an earlier stage of the process.

In the final phase, the target bed temperature of approximately 150 – 155 °C is reached after a similar duration for both flow rates. However, the lower mass flow rate of 60 kg/h resulted in diminished axial temperature differences, indicating more uniform heating. This effect is attributed to two factors: firstly, the increase in gas–solid contact time, and secondly, the enhancement of heat conduction, which contributes to temperature equalization at lower flow rates.

Overall, lower air flow results in slower but more uniform heating, whereas higher flow rates enhance convective heat transfer, leading to faster heating near the inlet, larger axial temperature gradients, and a longer time required for full thermal stabilization of the bed.

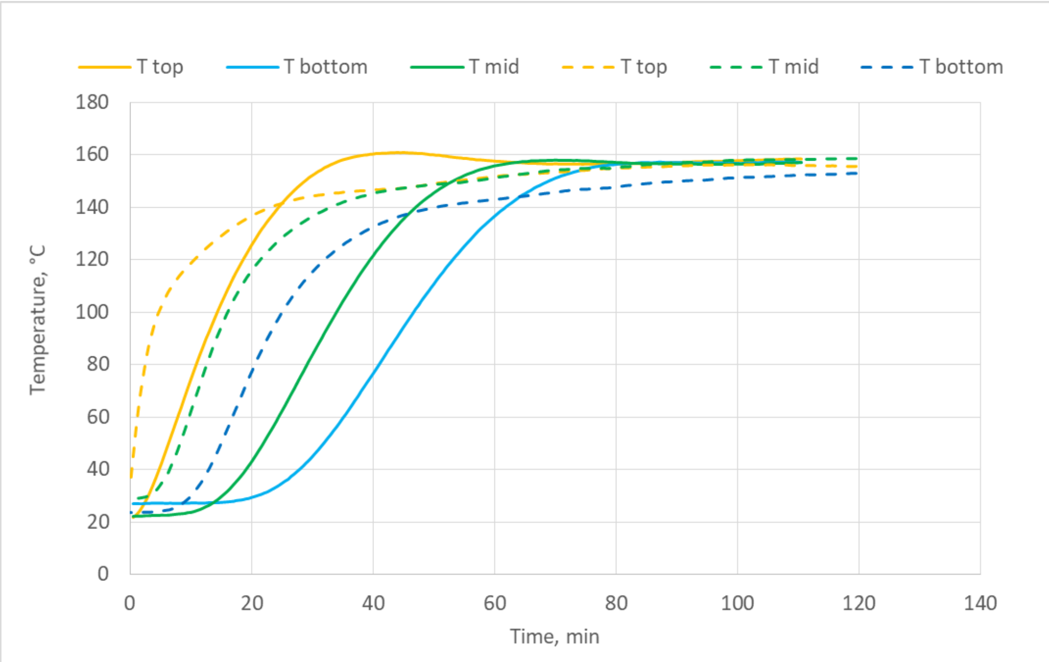


**Figure 12** Temperature distribution along the axis of the bed during charging. Air flow rates of 60 kg/h (solid line) and 120 kg/h (dashed line).

(a)

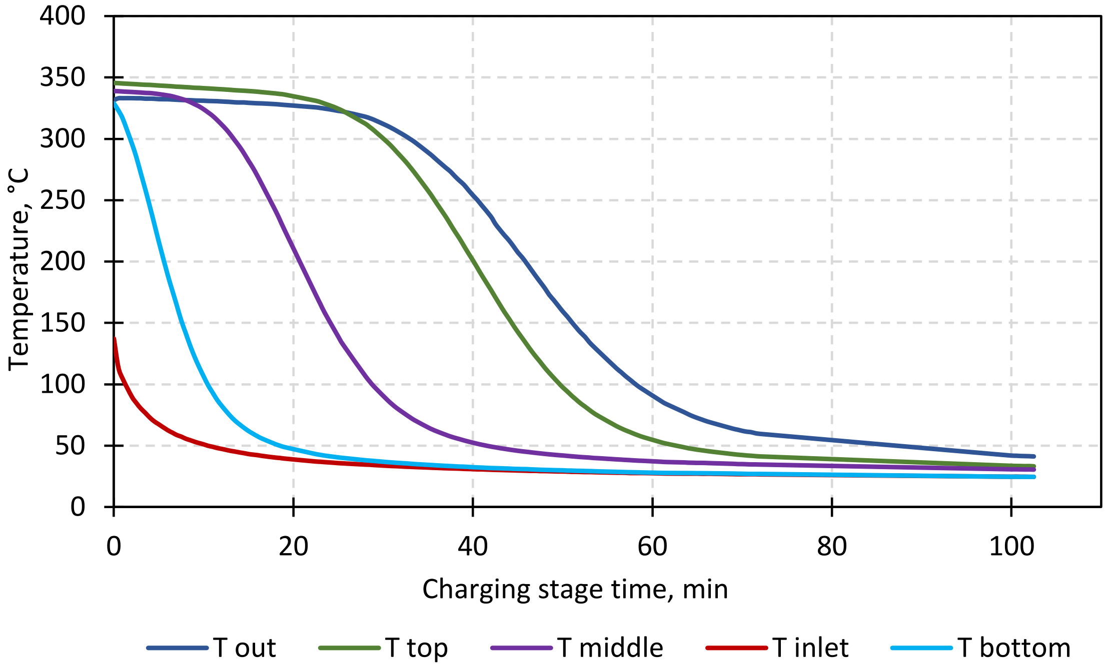
400
350
300
250
200
150
100
50
0
Temperature, °C
0
20
40
60
80
100
Charging stage time, min
T out
T top
T middle
T inlet
T bottom

(b)

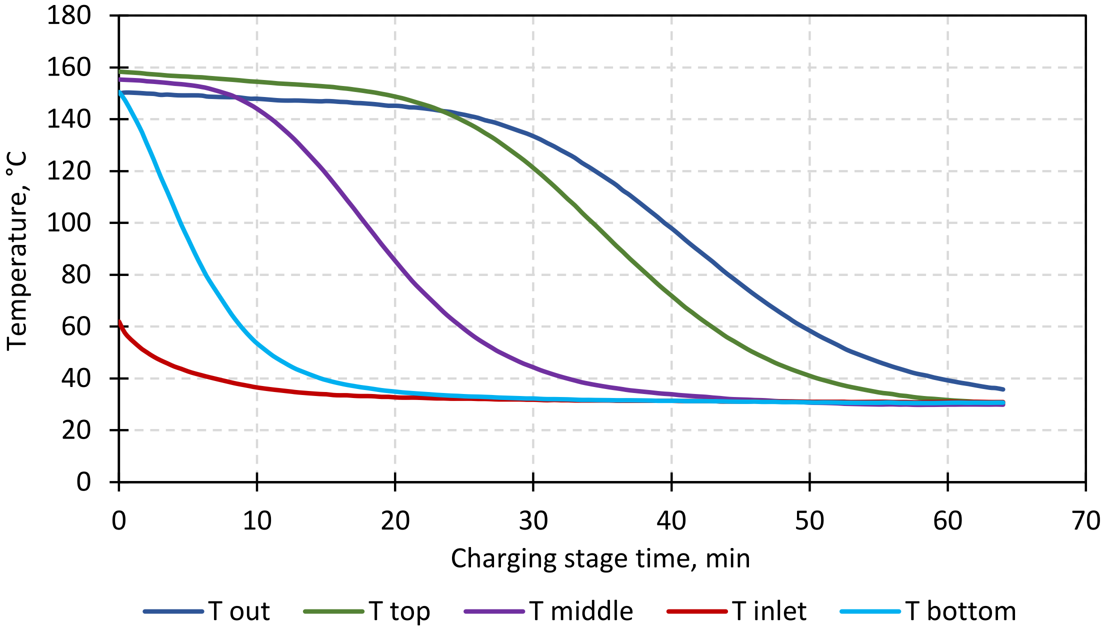


**Figure 13** Temperature distribution during the discharging of the storage tank for an air flow rate of 60 kg/h at different initial temperatures.

Figure 13 shows the temperature distribution during the discharging of the TES unit from two different initial (average) bed temperatures: 150 °C and 330 °C. In both cases, the air flow rate was 60 kg/h. The curves exhibit a similar overall behavior: the initial phase is characterized by a rapid temperature drop due to the large gradient between the hot bed and the cold inlet air. As cooling progresses, the temperature gradient decreases, resulting in a gradual flattening of the curves and a reduction in heat release rate.

The effective operating time of the TES unit depends on the chosen minimum useful outlet air temperature. For a threshold of $T_{out}$ > 50 °C, the operating time is approximately 55 minutes for an initial temperature of 155 °C and about 90 minutes for an initial temperature of 330 °C.

Moreover, as can be seen from Figure 13, doubling the initial bed temperature does not result in a proportional increase in the operating time of the storage system. With increasing initial temperature, both the total stored energy and the thermal power (P) increase, which limits the extension of effective operating time, as can be seen in Figure 14. The operating time is defined as the ratio of the released thermal energy to the heat output. Furthermore, a portion of the stored energy remains below the minimum useful air temperature and therefore cannot be utilized within the analyzed operating range.

Nevertheless, the maximum thermal power (heat output rate) of the bed discharged from 330 °C is approximately 2.5 times higher than that of the bed discharged from 150 °C. This difference directly results from the dependence of thermal power on the temperature difference between the air and the bed during discharge (ΔT).

$$P(t_i) = m_{air} C_{p\,air}(T_{out}(t_i) - T_{in}(t_i))$$

*P(tᵢ)* denotes the instantaneous thermal power.

Within the analyzed discharge range, the outlet–inlet air temperature difference for a bed discharged at 330 °C is approximately 2.5 times higher than that for a bed at 150 °C, resulting directly in a corresponding 2.5-fold increase in the maximum heat output.

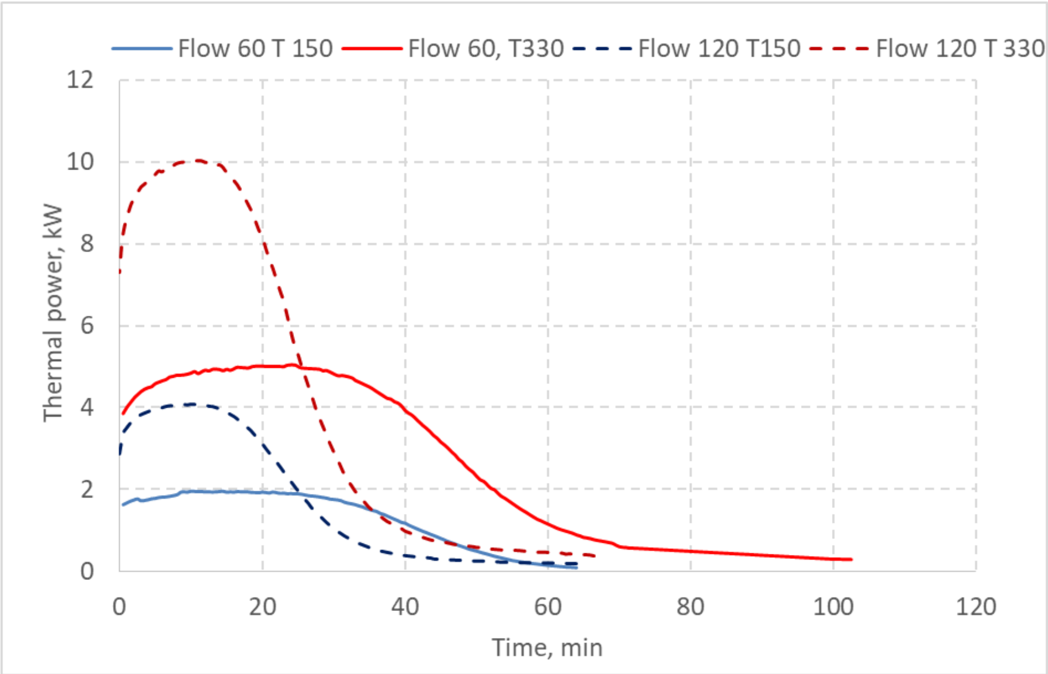


**Figure 14.** The heat output rate at various airflow rate and initial bed temperatures.

Furthermore, Figure 14 shows the effect of air mass flow rate on the achieved thermal power. It clearly visible, that increasing the airflow significantly raises the maximum heat output during the discharge TES unit, regardless of the initial bed temperature. This behavior directly follows from the definition of thermal power, whereby an increased air mass flow rate leads to an enhanced rate of heat recovery from the bed.

At a flow rate of 60 kg/h, the maximum power is approximately 2 kW for an initial temperature of 150 °C and about 5 kW for 330 °C. When the flow rate is increased to 120 kg/h, the maximum thermal power rises to approximately 4 kW at 150 °C and nearly 10 kW at 330 °C, demonstrating an almost proportional increase in maximum discharge power with mass flow rate.

At the same time, higher airflow leads to a significant reduction in the effective discharge time. The increased heat transfer rate results in faster cooling of the bed and a more rapid decline in power over time. Consequently, the stored thermal energy is released over a shorter period but at a higher instantaneous power.

The final results of the sensible heat storage experiments carried out by ITPE in Zabrze are presented in Table 3. The round-trip energy efficiency of the TES unit ($\eta_{en}$), defined as the ratio of the thermal energy recovered during discharge to the energy supplied during charging, ranges from 84% to 95% and exhibits only a moderate dependence on operating conditions. Slightly higher efficiency values are observed at increased air mass flow rates and higher initial bed temperatures, indicating that intensified heat transfer during both charging and discharging reduces relative heat losses over the storage cycle. These results confirm the high round-trip efficiency of the tested TES system and the internal consistency of its energy balance.

**Table 3.** Experimental data on energy storage in a basalt bed (obtained in ITPE).

| Average airflow rate, charging/discharging, kg/h | Average Temperature of the bed, °C | Charging | | Discharging | | Efficiency of TES $\eta_{en}$, % |
|---|---|---|---|---|---|---|
| | | $Q_{in}$, kWh | $P_{av}$, kW | $Q_{out}$, kWh | $P_{av}$, kW | |
| 60/61 | 155 | 1.58 | 0.86 | 1.38 | 1.29 | 87.30 |
| 120/121 | 153 | 1.92 | 0.97 | 1.82 | 1.71 | 94.60 |
| 60/61 | 338 | 5.25 | 1.36 | 4.41 | 2.58 | 84.00 |
| 106/122 | 330 | 5.45 | 1.67 | 4.65 | 4.20 | 85.50 |

Figure 15 presents the evolution of the state of charge of the thermal energy storage unit with a fixed storage bed during the experimental charging stage for different air mass flow rates.

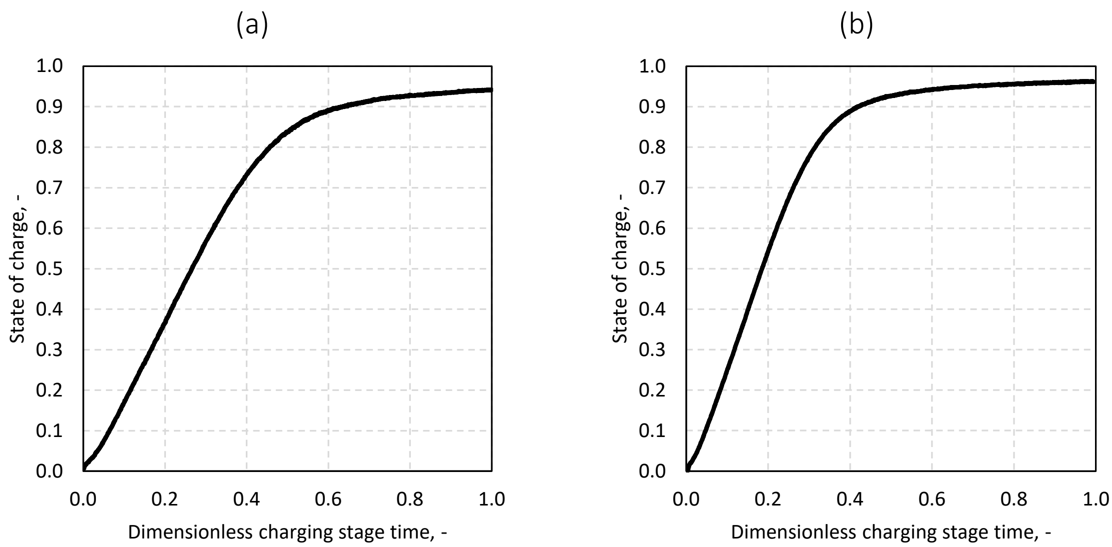

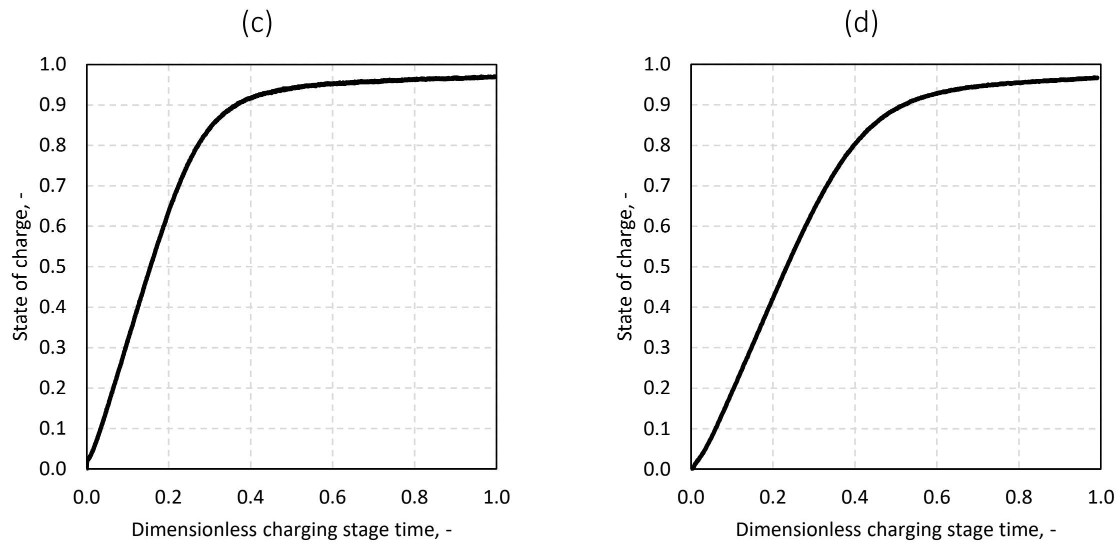


**Figure 15** Variation of the thermal energy storage unit's state of charge over the course of different experimental measurements.

Analyzing the results presented in Figures 15 (a) – 15 (b), a key relationship can be observed, which was incorporated into the simplified thermodynamic studies of the A-CAES system within WP4: namely, an almost linear increase in the state of charge (SOC) of the thermal energy storage unit up to approximately 0.70 – 0.80 during the charging stage. Furthermore, the SOC increases more rapidly with higher air mass flow rates, which directly corresponds to the amount of heat delivered to the storage unit volume. This observation confirms the authors' earlier findings regarding the possibility of distinguishing two sub-phases within the charging stage [32]. It should be noted, however, that the experimental studies provided only a one-dimensional temperature distribution of the storage material. Neglecting the radial temperature distribution of the basalt leads to an overestimation of the SOC parameter.

The change in the rate of SOC increase beyond the conventional threshold is primarily due to a decrease in the heat flux exchanged between the air and the rock material, caused by a reduction in the temperature difference between these phases in the upper layers of the storage bed. The temperature of the storage material in the lower parts of the unit continues to rise along with increasing outlet losses from the TES unit (Equation X). From the perspective of implementing this type of storage unit in a full-scale A-CAES system utilizing a post-mining shaft, an increase in air temperature from the TES during the discharging stage is undesirable, as higher gas temperatures in the compressed air reservoir could compromise the structural strength of the concrete shaft lining.

For this reason, in the A-CAES system modeling carried out within WP4, an excess volume of the thermal energy storage unit was assumed relative to the actual amount of heat to be stored, which effectively limits outlet losses during the charging stage. The methodology for determining the SOC transition point during charging was also implemented in the thermodynamic models developed as part of WP4.

## 4.2. Experimental analysis - Latent heat storage

As part of the project, ITPE investigated the processes of storing sensible heat using basalt and the process of storing latent heat using PCM (phase change material). Of the many materials previously reviewed [24], a mixture of sodium nitrate and potassium nitrate (Solar Salt) was selected. The parameters are listed in Table 4.

**Table 4** Parameters of studied Solar Salt [33], [34].

| PCM | Melting point | Latent heat | Specific heat capacity | Density | Thermal conductivity | |
|---|---|---|---|---|---|---|
| 60% $NaNO_3$<br>40% $KNO_3$ | 220-223°C | 113-117 J/g | 1.58-1.60 J/g·K | 1.71 (565 °C) | 0.55 | [33], [34] |
| | 226-228°C (melting)<br>219.7-219.9 (solidification) | 118-120 J/g (solidification) | - | - | - | ITPE's own research |

The PCM was obtained as follows: first, potassium nitrate, $KNO_3$ (pure) and sodium nitrate, $NaNO_3$ (pure) were dried in an oven at 105 °C. Then, they were then pre-crushed using a blade mill. Weighed quantities of the two salts were mixed and melted in a steel vessel in a muffle furnace at 350 °C. The molten PCM was then poured into aluminum cases. The necks of the aluminum cases were crimped using a press to seal them.

The melting point and latent heat of the resulting PCM were verified by TG-DSC analysis (Figure **16**). Portions of the previously prepared PCM were used for these tests (i.e., the PCM was melted and then solidified, cooled, and crushed into a powder). The data are collected in the Table 4. TG-DSC tests were performed using a Netzsch STA 409 PG Luxx thermobalance with a DSC holder. The heating and cooling temperature range was selected to cover the melting and solidification temperatures. Tests were conducted in an inert atmosphere of argon. The peaks corresponding to the melting and solidification of the samples were integrated on the recorded DSC curves, and the amount of heat absorbed during melting and released during solidification was measured. The heat of transition values were determined as the average value of at least two integrals. As can be seen, the phase transition temperatures and enthalpy of phase transition are consistent with the literature data.

In addition, the stability of the obtained PCM was verified by heating the composition at various temperatures, from 300 to 500 °C. Each temperature (300, 400, and 500 °C) was maintained for 3 hours. After each time interval, it was checked for loss of mass. The measurements were carried out in an air atmosphere, and the material was heated in an open vessel to allow for possible gas escape and evaporation. The mass loss was less than 0.5%.

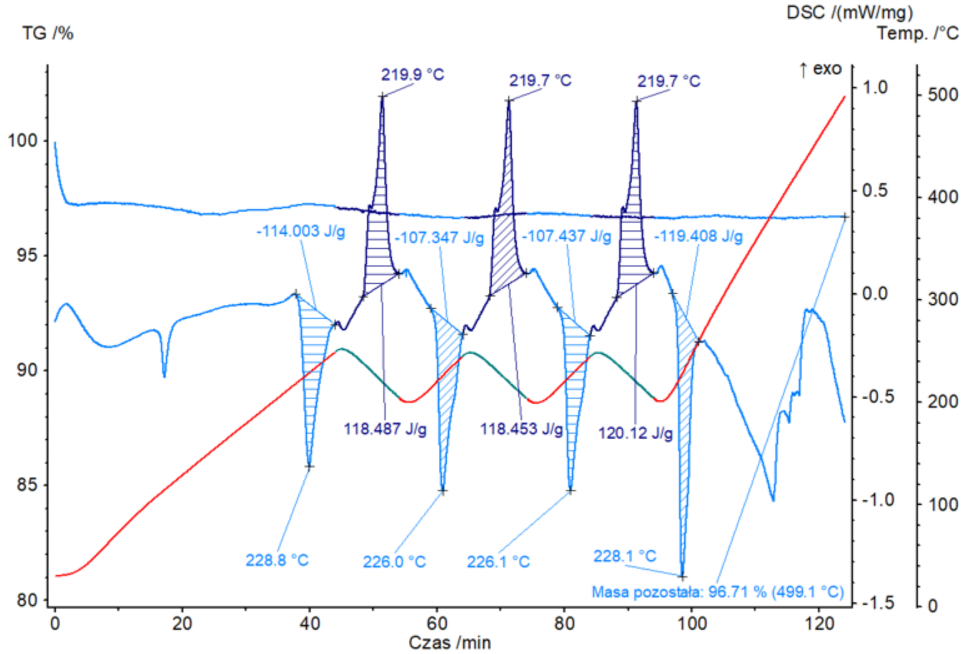


**Figure 16**. TG-DSC analysis for Solar Salt.

A similar process to verify the stability of the PCM was conducted on a small sample using thermogravimetric analysis (TG). The tests showed no significant weight loss (3.29%, according to TG analysis), confirming that the obtained PCM is stable up to 500 °C. Considering the phase transition temperature, PCM - Solar Salt can operate at temperatures ranging from approximately 230 °C to 500 °C.

Figure 17 shows the temperature profile of the bed during PCM energy storage charging. The target temperature of the bed was approximately 300 °C. Graph A shows the heating profile for a hot airflow of 60 kg/h, and Graph B shows the profile for an air flow of 106 kg/h.

(a)

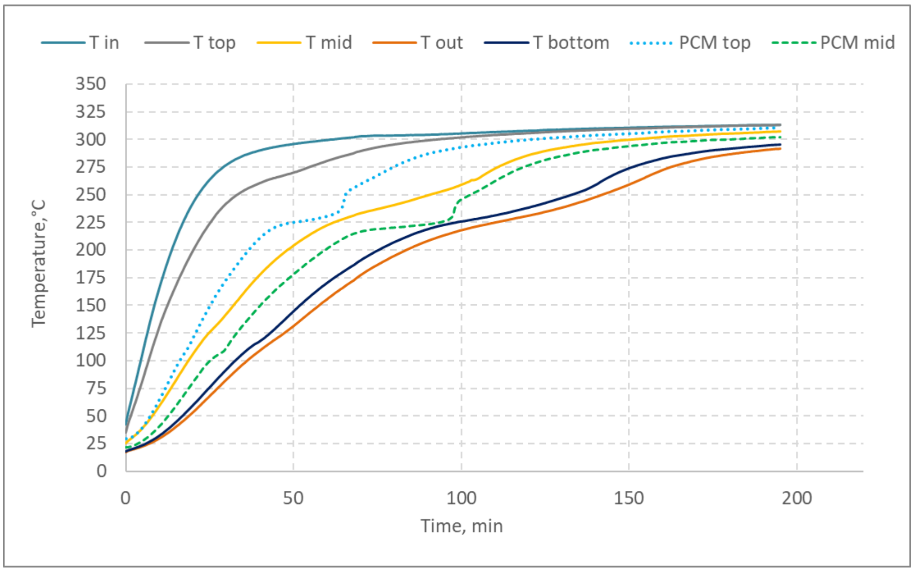

(b)

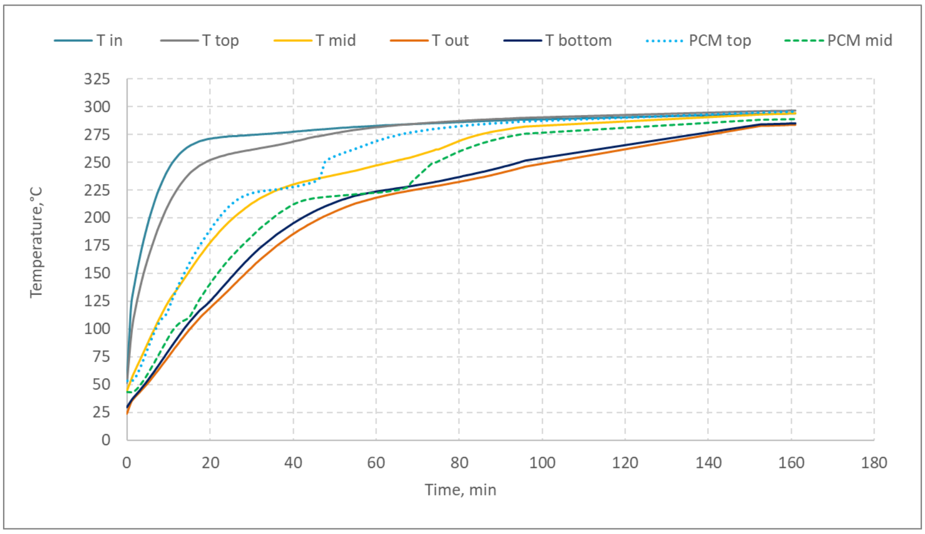


**Figure 17**. Loading of the Solar Salt storage for an air flow of 60 kg/h (a) and 105 kg/h (b) to a temperature of 300 °C.

In both cases, the bed gradually heats up from bottom to top, with the fastest temperature increase occurring in the upper part. The temperature curves measured inside the PCM capsules (dashed lines) show clear flattening between 220 °C and 225 °C, which corresponds to the phase transition temperature of solar salt (220 °C). This confirms the dominant role of latent heat storage and the local limitation of the PCM temperature increase rate during melting.

At higher airflow rates (106 kg/h), the temperature plateau associated with the phase transition is shorter, and PCM transitions to a liquid state faster and more uniformly along the bed. This indicates improved heat exchange intensity between the air and PCM capsules, as well as more efficient storage capacity utilization during charging.

Figure 18 shows the temperature profile of the PCM bed during the discharge phase of energy storage, starting from an initial bed temperature of approximately 300 °C. Figure A corresponds to an airflow rate of 60 kg/h, and Figure B corresponds to an airflow rate of 120 kg/h. In both cases, the temperature of the bed gradually decreases as the cooling front propagates from the cold air inlet. The temperature curves measured inside the PCM capsules (dashed lines) demonstrate a significant temperature drop within the 210 – 230 °C range, which corresponds to the solar salt phase transition temperature. This plateau indicates the release of latent heat and stabilization of the PCM temperature during the phase transition.

Increasing the airflow rate from 60 to 120 kg/h significantly reduces storage discharge time and accelerates the PCM's transition through the phase change range. This effect is clearly visible in the change in thermal power shown in Figure 19.

(a)

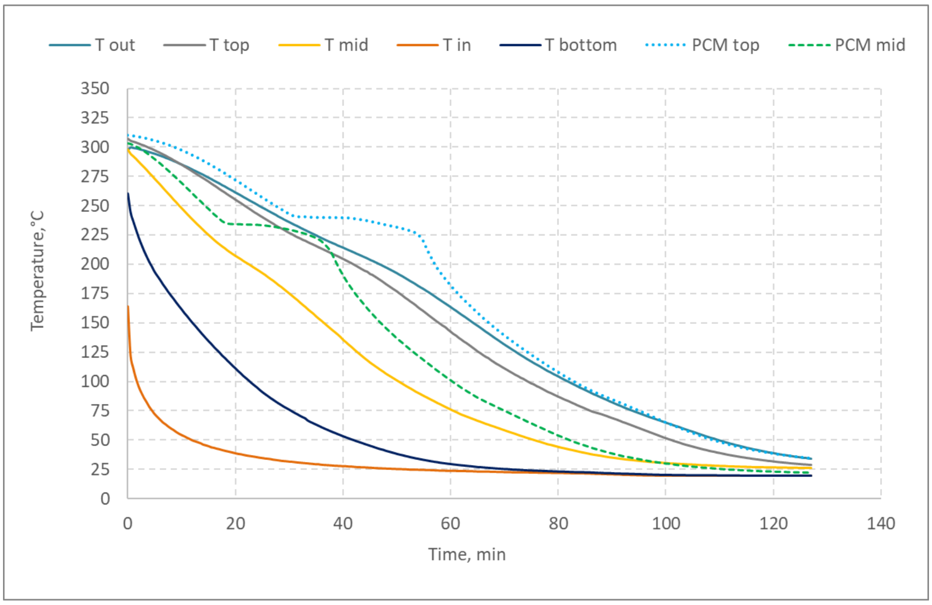


(b)

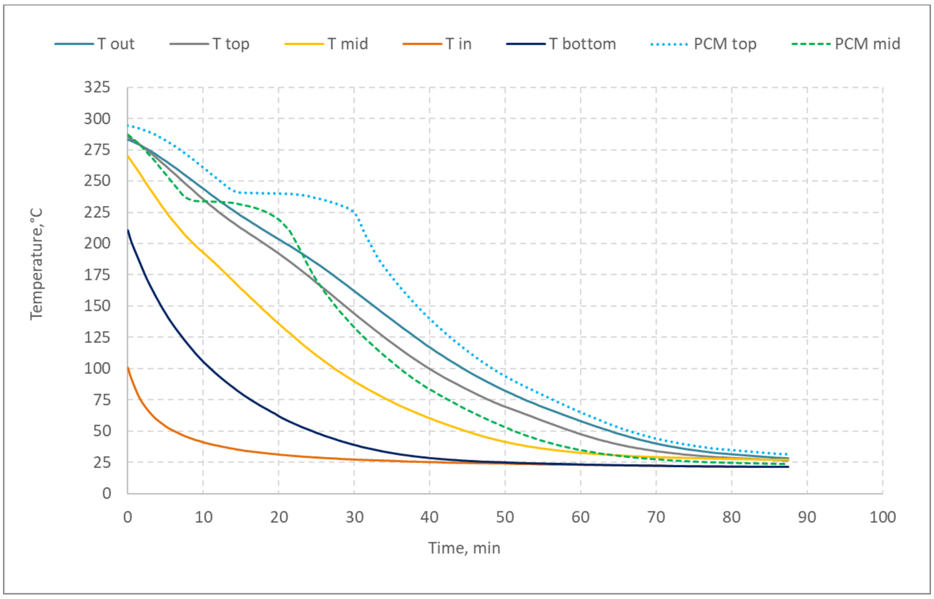


**Figure 18.** Solar Salt storage unloading for air flow rates of 60 kg/h (a) and 120 kg/h (b) from a temperature of approx. 300 °C

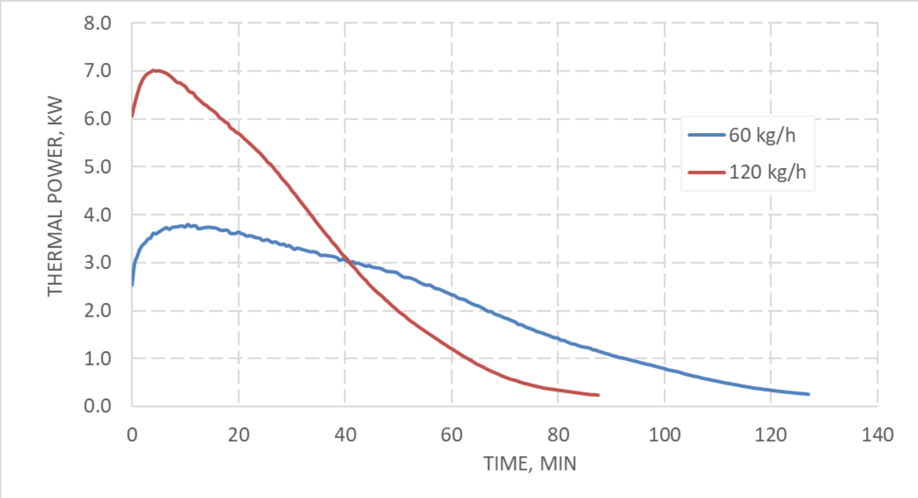


**Figure 19.** Heat output for discharging the Solar Salt storage tank from a temperature of 300 °C, for two different air flows.

Increasing the airflow significantly increases the maximum thermal power. For example, the maximum thermal power is 7 kW at a flow rate of 120 kg/h, compared to 3.8 kW at a flow rate of 60 kg/h (see Figure 19). Higher flow rates result in faster maximum power output and a more rapid decrease in power over time. This indicates more intensive energy absorption and a reduction in the effective discharge time of the storage unit. At lower flow rates, lower but more extended power characteristics are observed, corresponding to a longer, more stable heat transfer process.

Studies were also conducted on the discharge of the bed from a temperature of 400 °C (average bed temperature). To this end, the bed was heated to the target temperature (410 – 430 °C), and the temperature profiles are presented in Figure 19; the airflow was approximately 50 kg/h. Due to installation limitations (heat losses on the heating column), a higher airflow did not allow the column bed to reach the desired temperature.

The heating process to 400 °C is qualitatively similar to the bed charging profile to 300 °C; the main difference is the extension of the final heating phase to a higher target temperature. When charging to a higher temperature, a shorter temperature plateau is observed inside the PCM capsules within the phase transition temperature range. This indicates increased heat exchange between the hot air and the PCM bed.

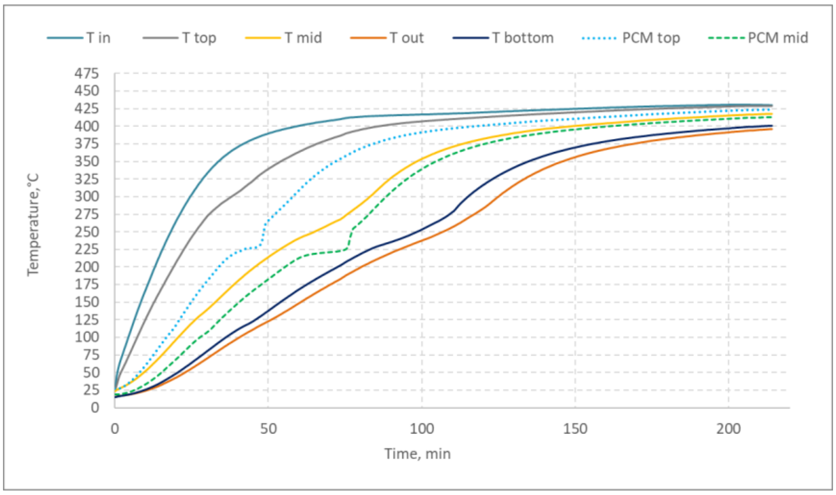


**Figure 20**. Charging the Solar Salt storage to 400 °C (air flow 50 kg/h).

(a)

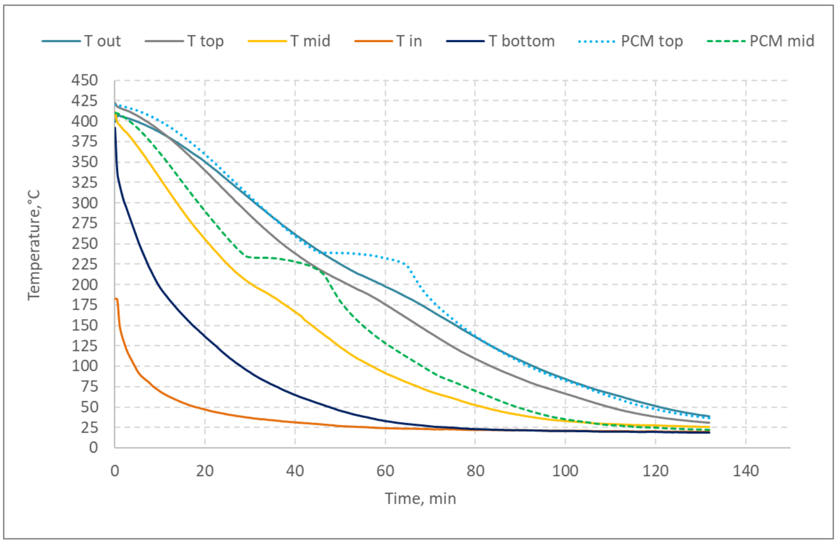


(b)

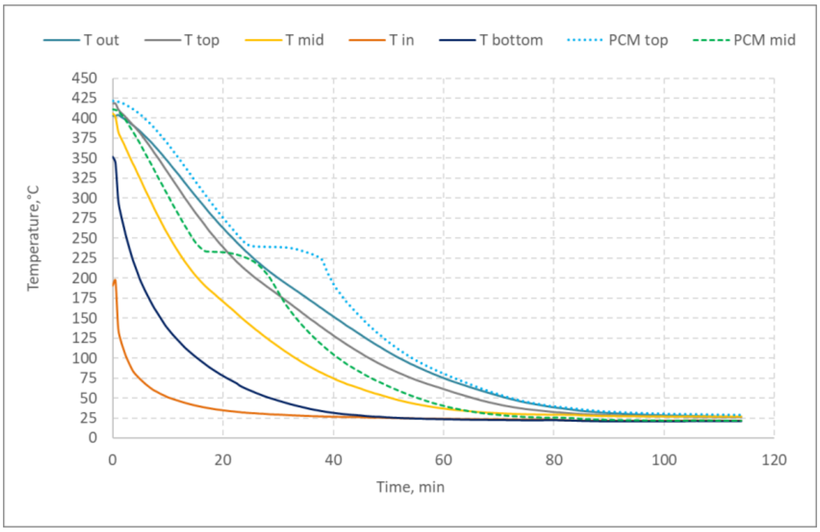


**Figure 21.** Unloading the Solar Salt storage tank for air flow rates of 60 kg/h (a) and 120 kg/h (b) from a temperature of approx. 300°C.

As shown in Figure 21, unloading a bed heated to approximately 400 °C exhibits similar dependencies on airflow as unloading the storage unit at 300 °C. This means that a higher flow rate results in a shorter unloading time and more efficient heat exchange. However, the unloading process from 400 °C takes longer than unloading from 300 °C while maintaining a similar PCM temperature plateau within the phase transition range. This results from the same latent heat release mechanism.

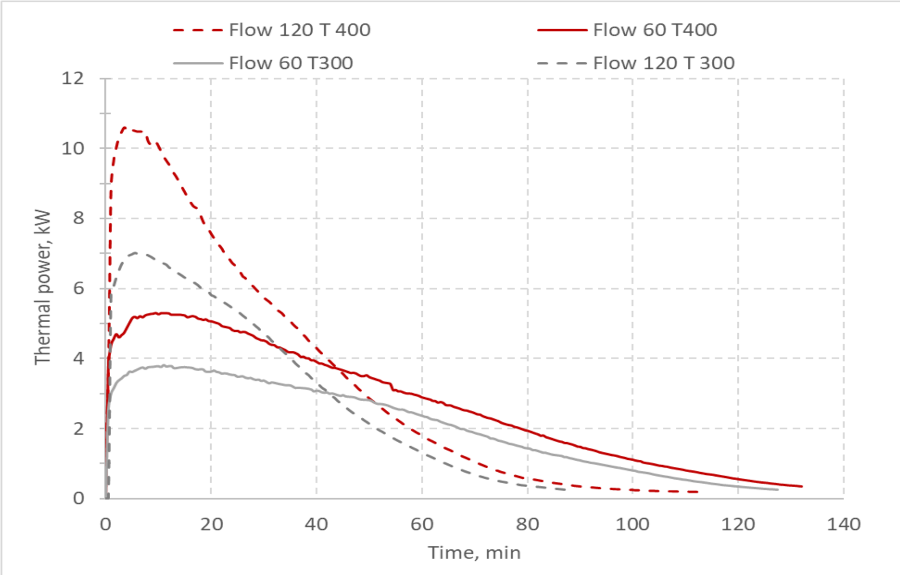


**Figure 22.** Comparison of thermal power for Solar Salt storage discharge depending on the initial storage temperature and air flow.

Figure 22 shows the change in heat power output over time for discharging the storage unit at 400 °C. For ease of comparison, the graph also shows the heat power curves from previous discharge tests conducted at 300 °C. The observed relationships are analogous to those obtained in previous studies. In all cases, the thermal power maximizes in the initial discharge phase and then systematically decreases as the temperature difference between the bed and the air decreases and the stored energy is depleted.

Increasing the airflow significantly increases the maximum heat output and results in a steeper curve over time due to intensified convective heat transfer and faster heat removal. Conversely, higher flow leads to a faster decrease in power and a shorter effective discharge time. Lower flow limits instantaneous power but allows for a longer, more even energy release process.

In order to compare a storage unit based on sensible heat (basalt) with the latent heat of PCM material, the instantaneous thermal power during the discharge of both types of storage units were presented at Figure 23. The initial temperature of both storage units  was in the range of 290 – 300 °C. The airflow rates were 60 kg/h and 120 kg/h.

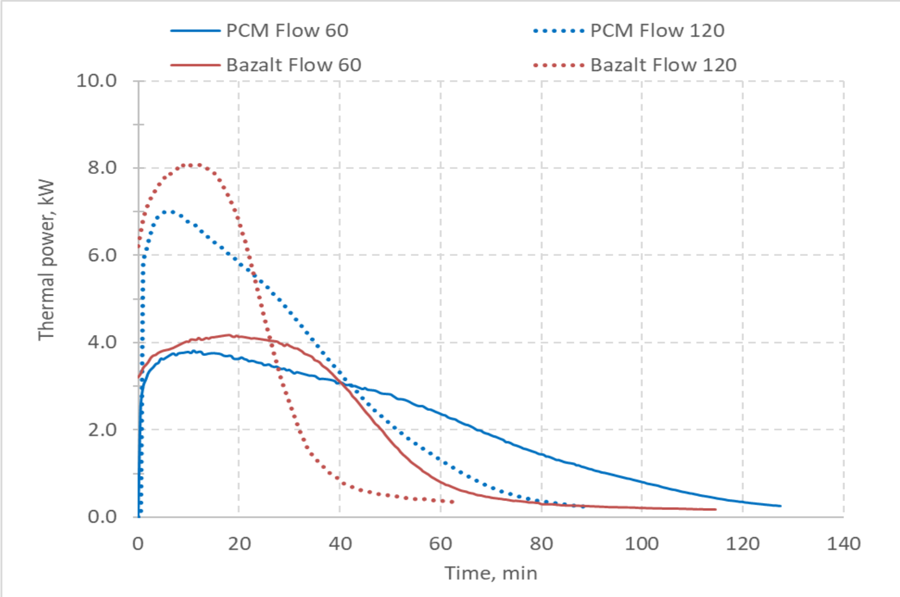


**Figure 23**. A comparison of the discharge power of a Solar Salt and a basalt storage unit.

Basalt-based storage has a higher maximum heat output during the initial discharge phase, particularly at higher air flow rates. However, basalt storage's heat output decreases rapidly over time due solely to the storage of sensible heat and the rapid decrease in temperature difference between the bed and the air. PCM storage has a lower maximum power output, but the energy release time is significantly longer due to the release of latent heat during phase changes and stabilization of the bed temperature. Consequently, PCM storage provides a more consistent and prolonged energy output, whereas sensible heat storage offers short-term, peaked power output.

It is also worth noting that the mass of the Solar Salt was lower than that of the basalt (28 kg versus 42 kg), due to differences in porosity. However, the volume of both beds was comparable (approximately 25 dm$^3$).

The table below summarizes the experimental results of the charging and discharging processes of the energy storage unit using PCM material.

**Table 5** Experimental data on energy storage in Solar Salt (obtained in ITPE).

| Average airflow rate, charging/discharging, kg/h | Average Temperature of the bed °C | Charging | | Discharging | | Efficiency of TES |
|---|---|---|---|---|---|---|
| | | $Q_{in}$, kWh | $P_{av}$, kW | $Q_{out}$, kWh | $P_{av}$, kW | $\eta_{en}$, % |
| 58/60 | 303 | 5.25 | 1.62 | 4.43 | 2.09 | 84.4 |
| 106/119 | 290 | 4.89 | 1.82 | 4.65 | 3.14 | 95.1 |
| 46/60 | 408 | 6.72 | 2.20 | 5.92 | 2.71 | 93.0 |
| 47/122 | 412 | 6.98 | 1.96 | 6.49 | 3.87 | 88.6 |

A comparison of the energy supplied to and recovered by the storage unit during charging and discharging, respectively, determined the total efficiency of the TES storage unit to be approximately 85 – 95%. This result confirms the high efficiency of the tested system. Slight differences in the obtained efficiency values are also due to the test stand's operating conditions. In particular, switching the installation between charging and discharging involved a short transition period of about 1 – 2 minutes, during which unavoidable heat losses occurred. Additionally, during discharge, the bed may not fully cool down, resulting in residual energy in the storage, which affects the determined cycle efficiency. Considering these factors, the results are representative of the PCM storage unit's actual operating conditions.

A comparison of the results for the PCM storage facility and the basalt-filled sensible heat storage facility reveals significant operational differences between the two. In PCM storage, the average discharge power is lower than in basalt storage (under similar temperature and airflow conditions), while the stored energy is higher. Latent heat plays an important role in PCM, contributing to a more stable charging and discharging process. In basalt storage, however, energy is stored exclusively as sensible heat, making it more dependent on the current temperature gradient.

The limitations of the stand prevent the study of PCM-LiNaK with a melting point of about 400 °C and the testing of thermal energy storage at 500 °C. The maximum set temperature tested for the heater in the heating column was 570 °C, and the airflow was 50 kg/h. This allowed the heating bed to reach a temperature of 410 – 420 °C.

## 4.3. Numerical modelling – sensible heat storage

The numerical investigations of the thermal energy storage unit were preceded by a model validation process using experimental data on the temperature rise of the storage material at the measurement points. The results are presented in Figures 22 (a) – (b).

(a)

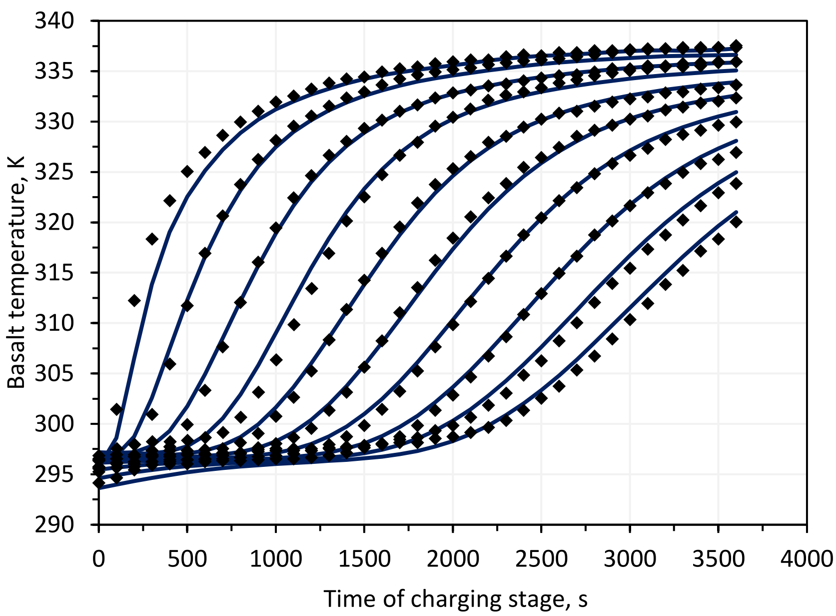


(b)

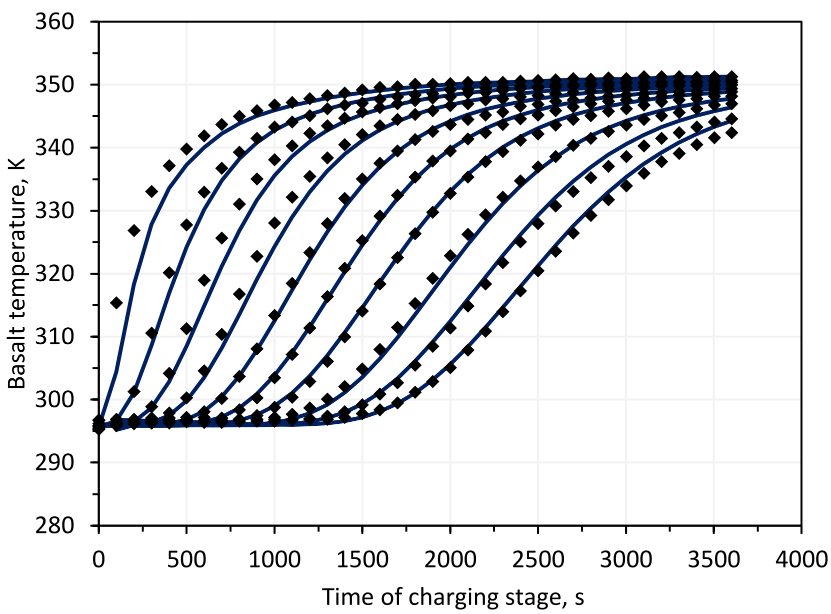


**Figure 24** Comparison of simulation and experimental results for: (a): $\dot{m} = 203.99$ kg/h, $T_{max} = 338.35$ K; (b): $\dot{m} = 264.05$ kg/h, $T_{max} = 352.75$ K.

The presented results indicate that the numerical model developed in ANSYS Fluent demonstrated sufficient accuracy when compared to the experimental data. Within the numerical investigations of the thermal energy storage unit with a porous bed, a multi-variant analysis was performed at the laboratory scale, and calculations were also conducted for a full-scale unit.

For the laboratory-scale TES numerical studies, analyses were carried out for charging and discharging stage durations ranging from 10 to 60 minutes, and for air mass flow rates between 0.025 kg/s and 0.040 kg/s, corresponding to the range employed in the experimental test rig operated by the Silesian University of Technology. For all simulations, the maximum air temperature was set at 100 °C. Figures 23 (a) – (d) show example temperature distributions of the rock material during the charging stage of the laboratory-scale thermal energy storage unit.

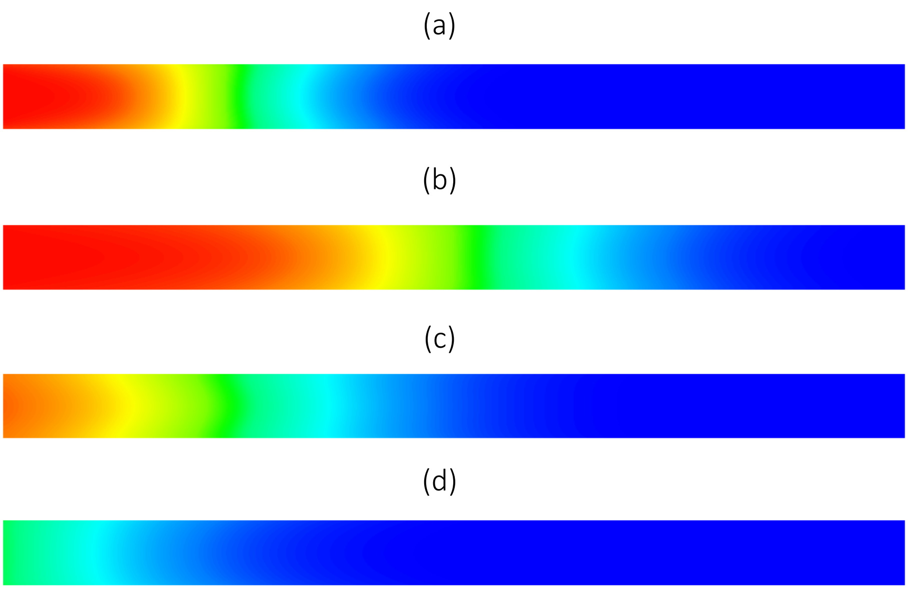


Figure 25 Temperature distribution of the storage material after: (a) 20 minutes; (b) 60 minutes; (c) 100 minutes; (d) 120 minutes.

Consistent with the experimental data, residual heat was also observed in the numerical simulations after the end of the discharging stage, resulting in higher basalt temperatures near the hot air inlet. The tables below present the calculated energy and exergy efficiencies of the cycle for all conducted numerical studies.

**Table 6** Values of the TES unit energy performance indicators for a mass flow rate of 0.025 kg/s.

| | Time of charging/discharging stages, min | | | | | |
|---|---|---|---|---|---|---|
| | 10 | 20 | 30 | 40 | 50 | 60 |
| Energy efficiency | 67.34% | 75.00% | 78.97% | 81.57% | 83.43% | 84.86% |
| Exergy efficiency | 29.34% | 38.33% | 43.14% | 46.33% | 48.59% | 50.28% |

**Table 7** Values of the TES unit energy performance indicators for a mass flow rate of 0.030 kg/s.

| | Time of charging/discharging stages, min | | | | | |
|---|---|---|---|---|---|---|
| | 10 | 20 | 30 | 40 | 50 | 60 |
| Energy efficiency | 69.06% | 76.36% | 80.12% | 82.57% | 84.35% | 85.88% |
| Exergy efficiency | 24.41% | 32.48% | 36.71% | 39.45% | 41.34% | 42.70% |

**Table 8** Values of the TES unit energy performance indicators for a mass flow rate of 0.035 kg/s.

| | Time of charging/discharging stages, min | | | | | |
|---|---|---|---|---|---|---|
| | 10 | 20 | 30 | 40 | 50 | 60 |
| Energy efficiency | 70.39% | 77.41% | 81.02% | 83.37% | 85.22% | 87.36% |
| Exergy efficiency | 18.60% | 25.86% | 29.55% | 31.86% | 33.40% | 34.48% |

**Table 9** Values of the TES unit energy performance indicators for a mass flow rate of 0.040 kg/s.

| | Time of charging/discharging stages, min | | | | | |
|---|---|---|---|---|---|---|
| | 10 | 20 | 30 | 40 | 50 | 60 |
| Energy efficiency | 71.51% | 78.29% | 81.77% | 84.11% | 86.41% | 89.59% |
| Exergy efficiency | 12.45% | 18.92% | 22.12% | 24.04% | 25.27% | 25.95% |

The multi-variant analysis of the laboratory-scale thermal energy storage unit revealed key characteristics of this type of system that must be considered in further studies of adiabatic compressed air energy storage within the HESS project.

The main conclusions include:

- An increase in the air mass flow rate leads to a higher calculated energy efficiency of the TES cycle. This effect is due to the increased air velocity, which enhances the heat transfer between the air and the storage material, thereby reducing the amount of residual heat remaining in the storage unit volume at the end of the discharging stage.
- An increase in the air mass flow rate results in a decrease in the calculated exergy efficiency of the TES cycle. This is due to the higher air velocity, which also increases the pressure drop across the system, confirming the results of the experimental investigations.

The figure below presents the temperature distribution of the storage material inside a full-scale TES unit operating within an adiabatic compressed air energy storage system, which is one of the components of the HESS system [17].

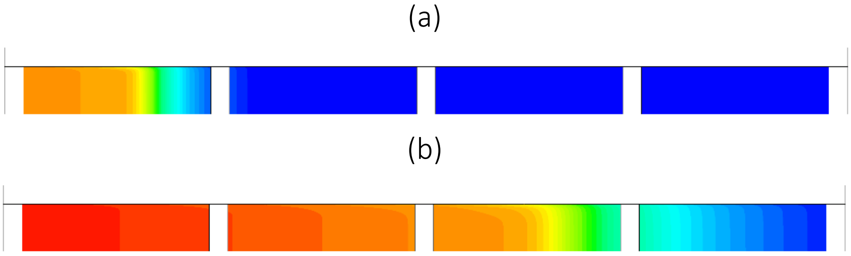


**Figure 26** Temperature distribution of the storage material in the full-scale thermal energy storage unit after: (a) 25% of the charging stage; (b) 100% of the charging stage.

The results presented in Figure 24 were obtained for the reference configuration of the A-CAES system, in which the compressed air reservoir (mine shaft) had a depth of 1000 meters and an internal diameter of 9 meters. The minimum pressure of the compressed air in the reservoir was 3.6 MPa, while the maximum at the end of the charging stage reached 5.0 MPa. The maximum expected temperature of the compressed air upstream of the TES unit was 500 °C.

As shown in Figure 24, no further increase in the temperature of the rock material was observed at the end of the charging stage, which is a result of the increased volume of the storage bed implemented to limit outlet losses. This indicates that the adopted methodology was appropriate from the perspective of A-CAES system operation. The maximum pressure drop recorded during the charging stage was 7.63 kPa, whereas during the discharging stage it reached 42.11 kPa. This difference resulted from the air mass flow rate being twice as high through the TES unit during discharging, as the discharging stage was assumed to last 4 hours, compared to 8 hours for the charging stage. The energy efficiency of the thermal energy storage unit for the presented configuration was approximately 96%.

## 4.4. Numerical modelling – latent heat storage

The graph shows the temperature evolution of the PCM capsule and the air flowing through the bed, as well as the phase change of the PCM over time. The red line represents the capsule temperature, the green line indicates the inlet air temperature to the bed, and the blue line shows the fraction of liquid PCM (0 – solid state, 1 – liquid state). Analysis of the graph indicates that the PCM material (Solar Salt) melts over approximately 429 seconds, or about 7 minutes. Complete heating of the capsule to the temperature of the flowing air, 300 °C, occurs after around 606 seconds, slightly over 10 minutes. The phase change curve shows gradual melting of the PCM as the capsule temperature rises. Once the material is fully liquid, further increase in capsule temperature approaches the inlet air temperature of 300 °C. Figure 25 shows the temperature during the charging stage. Figure 26 presents the temperature distribution during the charging stage. Figure 27 illustrates the fractions of solid and liquid phases.

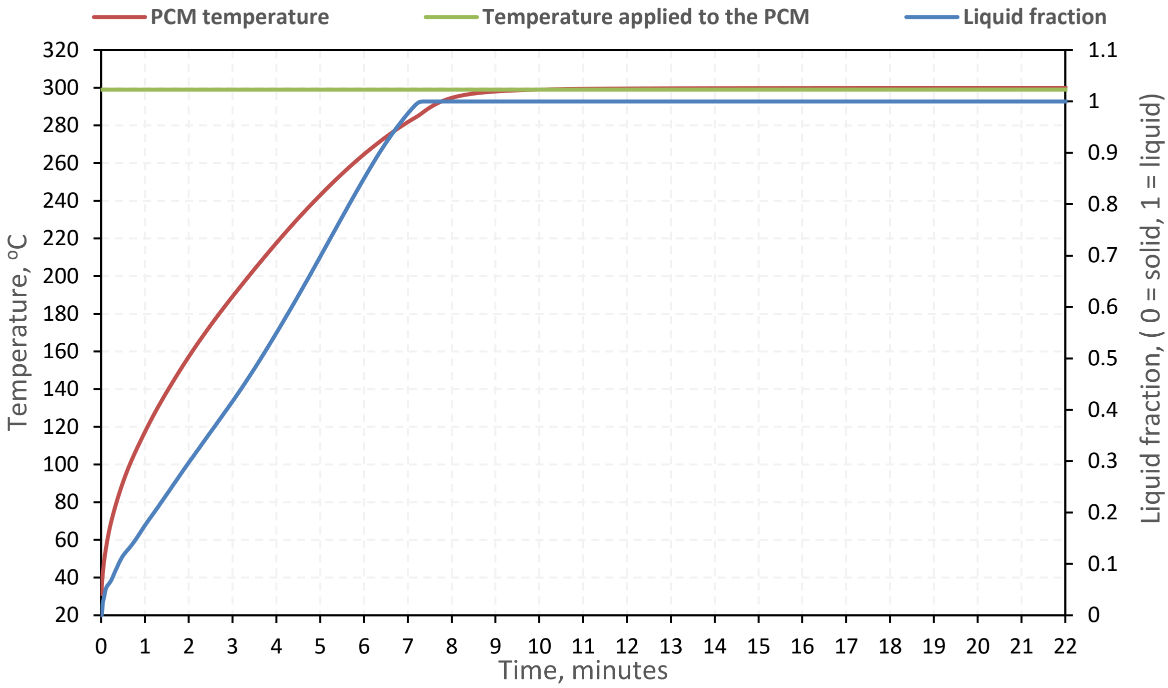


**Figure 27** Temperature during the charging stage.

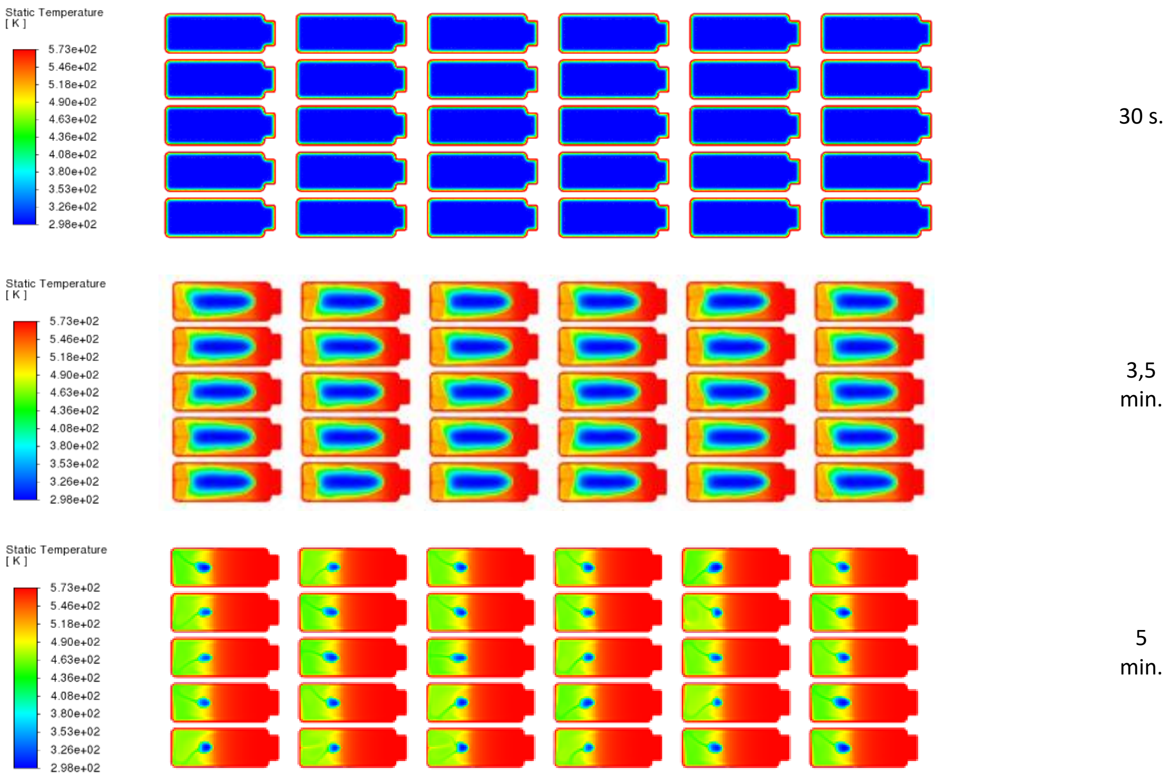

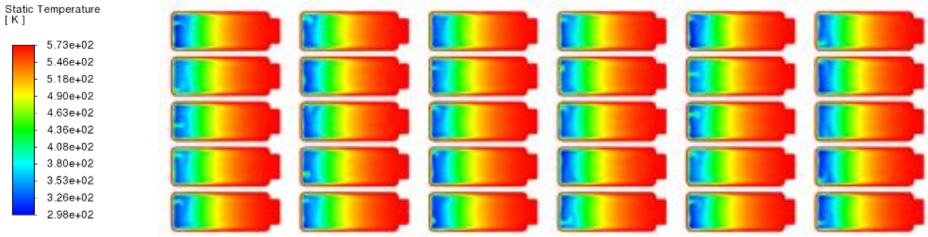


7 min.

**Figure 28** Temperature distribution during the charging stage.

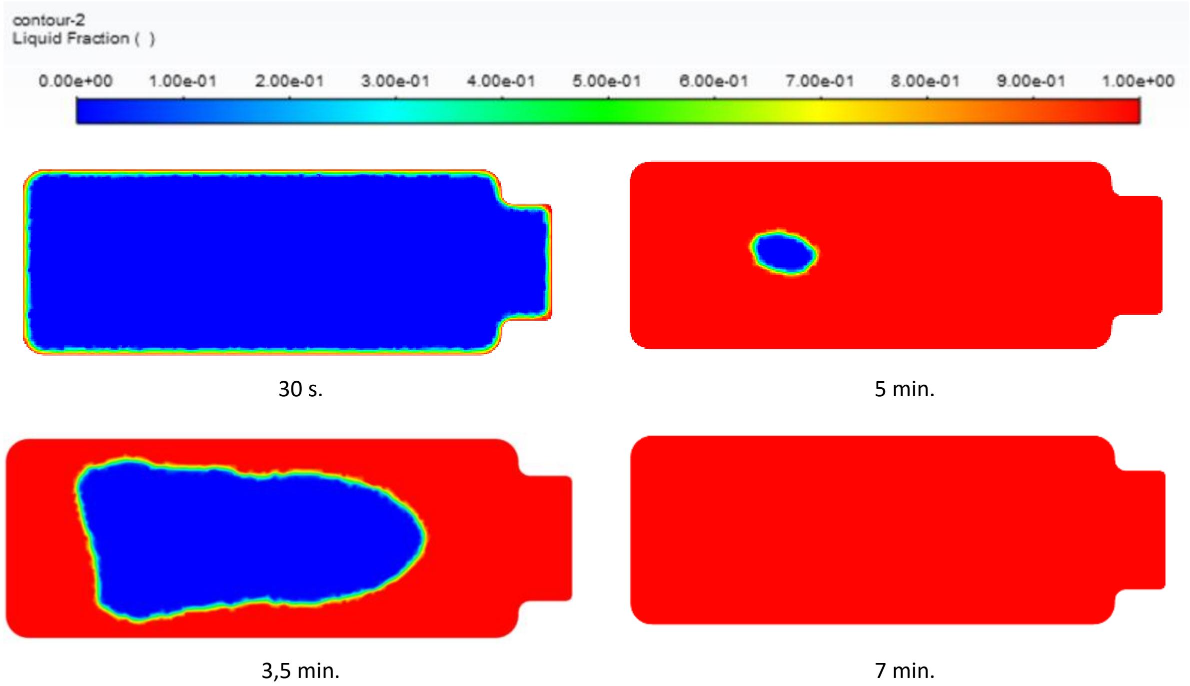


**Figure 29** Fractions of solid and liquid phases.

A temperature boundary condition of 300 °C was applied, surrounding the PCM capsule from all sides, resulting in uniform melting of the material. This is a significant simplification, as it does not fully replicate the actual temperature and melting profile, since the fluid flow is not considered. Consequently, the melting time is only about 7 minutes, and the temperature and melting profiles shown in Figures 25 and 26 are identical for each capsule.

During the first 30 seconds, the PCM begins to partially melt only in small areas near the surface, visible in photos as thin layers of molten material, while the interior remains solid. Over time, the molten liquid flows downward, forming a solid core in the central part of the capsule. After approximately 3.5 minutes, the core is still partially solid, while the outer layers are fully melted. Complete melting occurs around 7 minutes, corresponding to the point at which the maximum fraction of liquid is achieved throughout the capsule. At this stage, the capsule temperature asymptotically approaches the surrounding air temperature (300 °C), and the temperature distribution becomes uniform throughout the volume. The resulting visual temperature profile allows for identification of regions with varying heat transfer intensity, which is difficult to observe experimentally.

In the second variant, variant 1 was extended with a vertical column containing PCM bottles. The column is a model of the actual installation on which PCM heat storage measurements were carried out. In the column, air flows between the bottles, transferring heat to the surface of the bottles. In the extended model variant, which includes the geometry of the column and the air flow domain, 25 °C was set as the temperature of the bottles and the entire installation, and then 500 °C was set as the temperature of the air entering the column at the inlet. As in the first variant, the PCM material is solar salt (NaNO3-KNO3) with a melting temperature range of $T_{solidus}$ = 220 °C, $T_{liquidus}$ = 225 °C. The air velocity at the inlet is 0.5 m/s.

The PCM melting process begins when air flow with an inlet temperature of 500 °C is activated and lasts for approximately 180 minutes. The figure (Figure 30) shows a graph summarising the results.

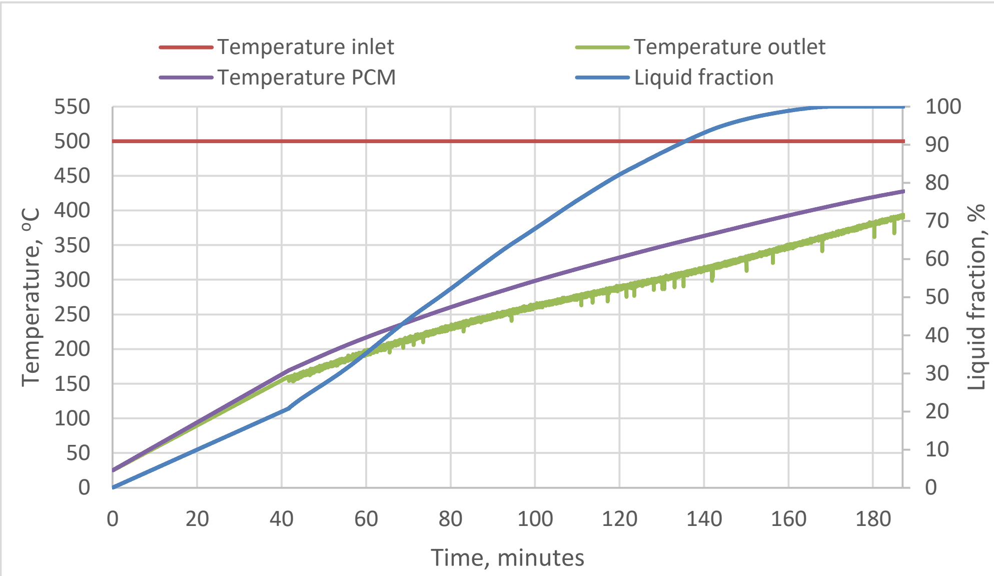


**Figure 30** Summary of results.

The horizontal axis of the graph shows time (min), the left vertical axis shows temperature (°C), and the right vertical axis shows the degree of liquefaction (%). The inlet air temperature remains constant at 500 °C throughout the simulation. The outlet air temperature rises from the initial value to approximately 400 °C, indicating intense heat absorption by the PCM bed. The average PCM temperature rises from the initial temperature to approximately 400 – 420 °C. The temperature distribution is shown in the figure (Figure 31).

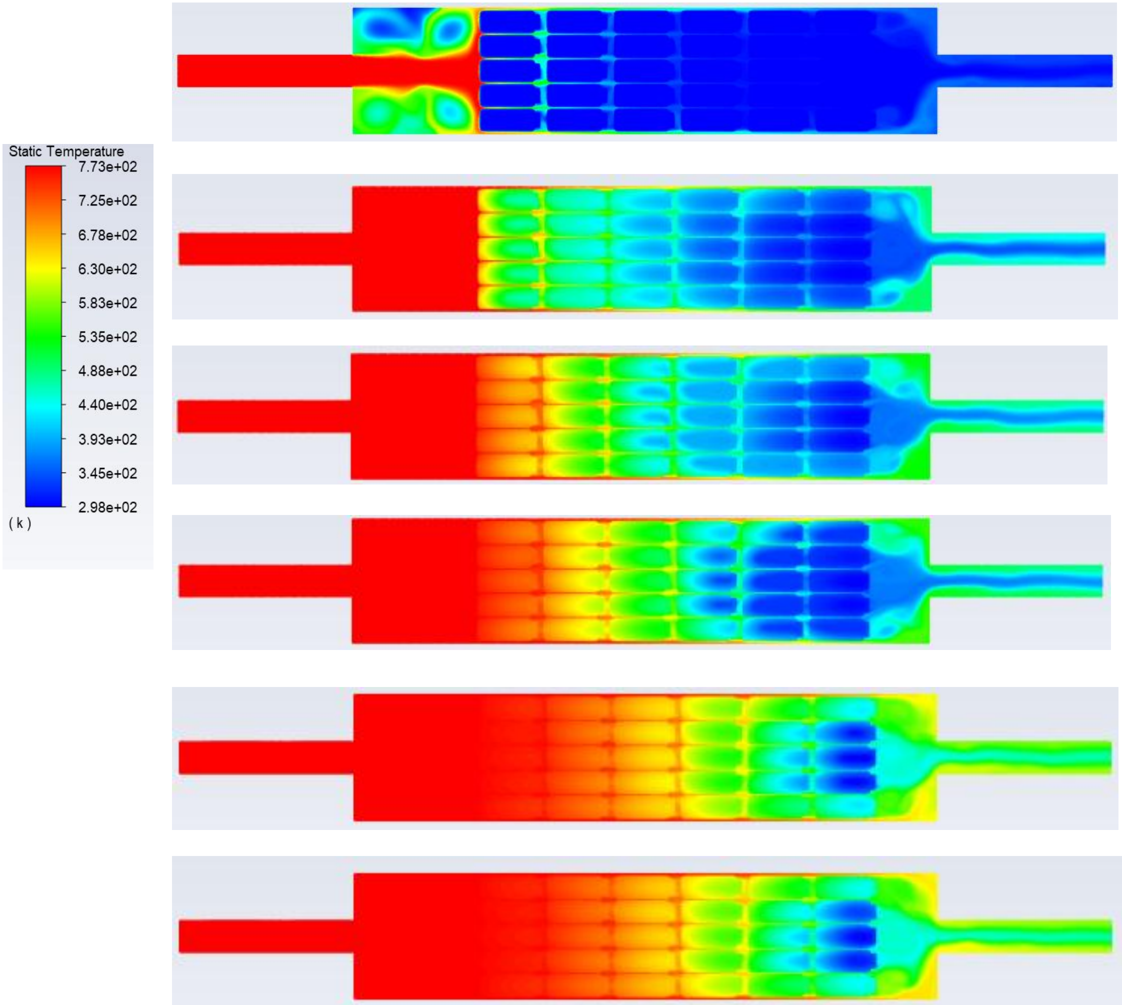


**Figure 31** Temperature distribution.

The figure (Figure 32) shows the flow profile in a steady state.

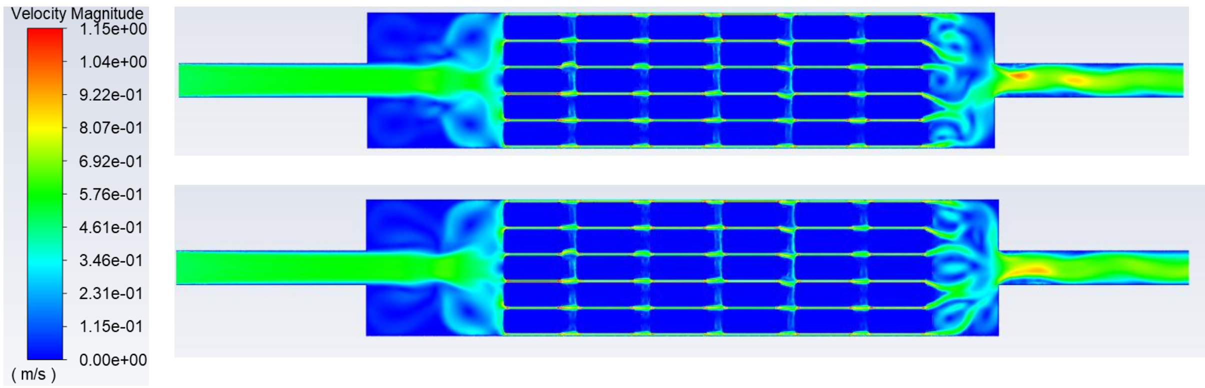


**Figure 32** Flow profile.

The distribution of the liquid fraction is shown in the figure (Figure 33). The degree of PCM liquefaction increases from 0% to a value close to 100%. The fastest melting occurs in the range of approximately 40 – 120 minutes, while after 160 – 170 minutes the material is practically completely melted. At the end of melting, the average temperature of the PCM is approximately 400 – 420 °C, and the temperature difference between the air inlet and outlet decreases, which means a decrease in the intensity of heat exchange. The results clearly indicate that the PCM bed melts completely in less than 3 hours of system operation under the specified flow and temperature conditions.

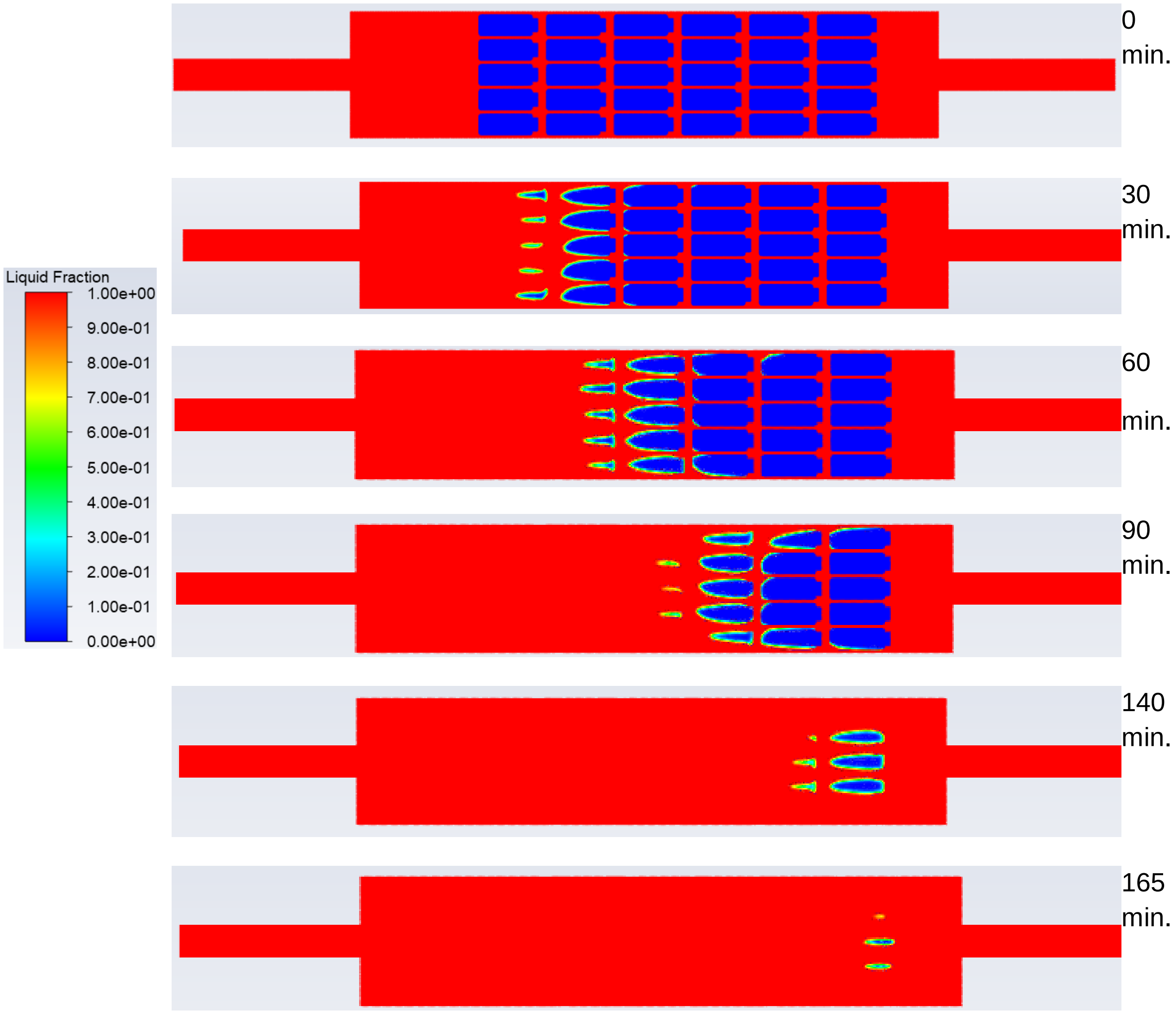


**Figure 33** Liquid fraction (red: liquid, blue: solid).

The first variant involved direct modelling of the bottle bed in the column, while the second variant presented a column heated by an air stream, in which the bed was replaced by an averaged model corresponding to the properties of the first variant. This approach made it possible to compare the impact of bed geometry on heat transfer and the PCM melting process while maintaining comparable boundary conditions.

# 5. Summary

As part of the implementation of WP5 within the HESS project, comprehensive multi-variant experimental investigations of thermal energy storage units with porous fillings were conducted. Thermal energy storage units constitute key components of the energy storage system proposed under the HESS framework, as they provide the core system functionalities and enable thermal integration of its individual subsystems. The studies carried out by research teams from the Silesian University of Technology and the Institute of Energy and Fuel Processing Technology employed materials capable of storing both sensible and latent heat, identified during earlier stages of the project.

The experimental and numerical investigations conducted led to the formulation of the following conclusions and recommendations for further work:

- It was observed that, for all experimental cases, the temperature of the storage material decreases along the axial direction toward the outlet of the thermal energy storage unit. Due to heat losses to the surroundings, it was not possible to achieve a uniform temperature distribution along the axis of the storage unit.
- The depletion of the storage capacity of the thermal energy storage unit is associated with intensive outlet losses. It is recommended to introduce an appropriate excess volume of the storage bed in order to mitigate this effect.
- The application of a rock bed with smaller particle size enhances the intensity of heat transfer between the air and the storage material; however, it also results in an increased air pressure drop.
- The state of charge of the thermal energy storage unit increases linearly during the charging stage up to a threshold of approximately 70–80%. Beyond this point, the rate of increase decreases significantly due to rising outlet losses.
- Numerical modeling performed in ANSYS Fluent was successfully validated against the experimental results.
- It was demonstrated that an increase in the air mass flow rate leads to an increase in the energy efficiency of the TES cycle. At the same time, due to the associated pressure drop, a decrease in overall energy efficiency is observed.
- Full-scale numerical modeling of a TES unit is feasible; however, multi-variant analyses are impractical due to the extremely long computation time of a single simulation cycle (approximately 130 hours). Full-scale numerical modeling of the TES unit confirmed the necessity of applying an excess volume of storage material to minimize outlet losses during the charging stage.

Ultimately, based on the analysis of experimental and numerical results, it was concluded that for thermal energy storage within an adiabatic A-CAES system, sensible heat storage in solid materials (natural rocks) is the preferred technology. This is primarily due to economic factors, as natural rocks are relatively inexpensive because of their widespread availability. Direct contact between the heat transfer medium and the storage material also reduces exergy losses. Previous studies have further shown that a large proportion of phase change materials are characterized by toxicity, which would pose a hazard in the context of operating a thermal energy storage system in a mining shaft. Selected phase change thermal energy storage systems may, however, play a key role as integrators of energy storage subsystems, for example through their installation within interstage heat exchangers of air compressors. The stored heat can then be used for additional air heating during the discharge stage.

# 6. References

[1] B. Talebjedi, T. Laukkanen, and H. Holmberg, ‘Integration of thermal energy storage for sustainable energy hubs in the forest industry: A comprehensive analysis of cost, thermodynamic efficiency, and availability’, *Heliyon*, vol. 10, no. 17, p. e36519, Sep. 2024, doi: 10.1016/j.heliyon.2024.e36519.

[2] R. I. Areola, A. A. Adebiyi, and K. Moloi, ‘Integrated Energy Storage Systems for Enhanced Grid Efficiency: A Comprehensive Review of Technologies and Applications’, *Energies*, vol. 18, no. 7, p. 1848, Apr. 2025, doi: 10.3390/en18071848.

[3] Q. Fu, Z. Xing, C. Zhang, and J. Xu, ‘A Review and Prospective Study on Modeling Approaches and Applications of Virtual Energy Storage in Integrated Electric–Thermal Energy Systems’, *Energies*, vol. 17, no. 16, p. 4099, Aug. 2024, doi: 10.3390/en17164099.

[4] W. Kosman, A. Rusin, and P. Reichel, ‘Application of an energy storage system with molten salt to a steam turbine cycle to decrease the minimal acceptable load’, *Energy*, vol. 266, p. 126480, Mar. 2023, doi: 10.1016/j.energy.2022.126480.

[5] D. Enescu, G. Chicco, R. Porumb, and G. Seritan, ‘Thermal Energy Storage for Grid Applications: Current Status and Emerging Trends’, *Energies*, vol. 13, no. 2, p. 340, Jan. 2020, doi: 10.3390/en13020340.

[6] S. Tetteh, G. Juul, M. Järvinen, and A. Santasalo-Aarnio, ‘Improved effective thermal conductivity of sand bed in thermal energy storage systems’, *Journal of Energy Storage*, vol. 86, p. 111350, May 2024, doi: 10.1016/j.est.2024.111350.

[7] K. Lepiksaar, V. Mašatin, E. Latõšov, A. Siirde, and A. Volkova, ‘Improving CHP flexibility by integrating thermal energy storage and power-to-heat technologies into the energy system’, *Smart Energy*, vol. 2, p. 100022, May 2021, doi: 10.1016/j.segy.2021.100022.

[8] X. Yu, W. Dou, Z. Zhang, Y. Hong, G. Qian, and Z. Li, ‘Performance Analysis and Optimization of Compressed Air Energy Storage Integrated with Latent Thermal Energy Storage’, *Energies*, vol. 17, no. 11, p. 2608, May 2024, doi: 10.3390/en17112608.

[9] Ł. Bartela, J. Ochmann, S. Waniczek, M. Lutyński, G. Smolnik, and S. Rulik, ‘Evaluation of the energy potential of an adiabatic compressed air energy storage system based on a novel thermal energy storage system in a post mining shaft’, *Journal of Energy Storage*, vol. 54, p. 105282, Oct. 2022, doi: 10.1016/j.est.2022.105282.

[10] E. Barbour, D. Mignard, Y. Ding, and Y. Li, 'Adiabatic Compressed Air Energy Storage with packed bed thermal energy storage', *Applied Energy*, vol. 155, pp. 804–815, Oct. 2015, doi: 10.1016/j.apenergy.2015.06.019.

[11] A. Gil, M. Medrano, I. Martorell, A. Lázaro, P. Dolado, B. Zalba, and L. F. Cabeza, 'State of the art on high temperature thermal energy storage for power generation. Part 1—Concepts, materials and modellization', *Renewable and Sustainable Energy Reviews*, vol. 14, no. 1, pp. 31–55, Jan. 2010, doi: 10.1016/j.rser.2009.07.035.

[12] M. Mersch, P. Sapin, A. V. Olympios, Y. Ding, N. Mac Dowell, and C. N. Markides, 'A unified framework for the thermo-economic optimisation of compressed-air energy storage systems with solid and liquid thermal stores', *Energy Conversion and Management*, vol. 287, p. 117061, Jul. 2023, doi: 10.1016/j.enconman.2023.117061.

[13] A. Ferre, S. Serra, J. Pouvreau, R. Manceau, A. Bruch, O. Soriano, and M. Bois, 'Experimental study of thermocline behavior under high propagation velocities in a water based thermal energy storage', *Journal of Energy Storage*, vol. 125, p. 116921, Jul. 2025, doi: 10.1016/j.est.2025.116921.

[14] D. W. Waples and J. S. Waples, 'A Review and Evaluation of Specific Heat Capacities of Rocks, Minerals, and Subsurface Fluids. Part 1: Minerals and Nonporous Rocks', *Natural Resources Research*, vol. 13, no. 2, pp. 97–122, Jun. 2004, doi: 10.1023/B:NARR.0000032647.41046.e7.

[15] C. Martin, A. Bonk, M. Braun, C. Odenthal, and T. Bauer, 'Investigation of the long-term stability of quartzite and basalt for a potential use as filler materials for a molten-salt based thermocline storage concept', *Solar Energy*, vol. 171, pp. 827–840, Sep. 2018, doi: 10.1016/j.solener.2018.06.090.

[16] J. Ochmann, K. Rusin, S. Rulik, S. Waniczek, and Ł. Bartela, 'Experimental and computational analysis of packed-bed thermal energy storage tank designed for adiabatic compressed air energy storage system', *Applied Thermal Engineering*, vol. 213, p. 118750, Aug. 2022, doi: 10.1016/j.applthermaleng.2022.118750.

[17] J. Ochmann, 'Analiza cieplno-przepływowa zasobnika ciepła ze złożem porowatym przewidzianego do zastosowania w adiabatycznym systemie magazynowania energii w sprężonym powietrzu'. Gliwice, 2025. [Online]. Available: https://bip.polsl.pl/

[18] 'Venture Industries Sp. z o. o.' Accessed: Dec. 01, 2025. [Online]. Available: https://www.venture.pl/

[19] 'Lenze Polska Sp. z o.o.' Accessed: Dec. 01, 2025. [Online]. Available: https://www.lenze.com/

[20] 'APLISENS S.A'. Accessed: Sep. 01, 2025. [Online]. Available: https://aplisens.pl/

[21] 'Leister Technologies LLC'. Accessed: Dec. 01, 2025. [Online]. Available: https://www.leister.com/

[22] 'Victaulic Company'. Accessed: Dec. 01, 2025. [Online]. Available: https://www.victaulic.com/

[23] 'Termoaparatura Wrocław'. Accessed: Dec. 01, 2025. [Online]. Available: https://termoaparatura.com.pl/

[24] M. Jurczyk, T. Spietz, A, Czardybon, S. Dobras, K. Ignasiak,Ł. Bartela, W. Uchman, and J. Ochmann, 'Review of Thermal Energy Storage Materials for Application in Large-Scale Integrated Energy Systems—Methodology for Matching Heat Storage Solutions for Given Applications', *Energies*, vol. 17, no. 14, p. 3544, Jul. 2024, doi: 10.3390/en17143544.

[25] P. Schwarzmayr, F. Birkelbach, H. Walter, and R. Hofmann, 'Exergy efficiency and thermocline degradation of a packed bed thermal energy storage in partial cycle operation: An experimental study', *Applied Energy*, vol. 360, p. 122895, Apr. 2024, doi: 10.1016/j.apenergy.2024.122895.

[26] M. Cascetta, G. Cau, P. Puddu, and F. Serra, 'A comparison between CFD simulation and experimental investigation of a packed-bed thermal energy storage system', *Applied Thermal Engineering*, vol. 98, pp. 1263–1272, Apr. 2016, doi: 10.1016/j.applthermaleng.2016.01.019.

[27] X.-L. Ouyang, R.-N. Xu, and P.-X. Jiang, 'Three-equation local thermal non-equilibrium model for transient heat transfer in porous media: The internal thermal conduction effect in the solid phase', *International Journal of Heat and Mass Transfer*, vol. 115, pp. 1113–1124, Dec. 2017, doi: 10.1016/j.ijheatmasstransfer.2017.07.088.

[28] N. Wakao, S. Kaguei, and T. Funazkri, 'Effect of fluid dispersion coefficients on particle-to-fluid heat transfer coefficients in packed beds', *Chemical Engineering Science*, vol. 34, no. 3, pp. 325–336, 1979, doi: 10.1016/0009-2509(79)85064-2.

[29] F. R. Menter, 'Two-equation eddy-viscosity turbulence models for engineering applications', *AIAA Journal*, vol. 32, no. 8, pp. 1598–1605, Aug. 1994, doi: 10.2514/3.12149.

[30] S. Younoussi and A. Ettaouil, 'Calibration method of the k-ω SST turbulence model for wind turbine performance prediction near stall condition', *Heliyon*, vol. 10, no. 1, p. e24048, Jan. 2024, doi: 10.1016/j.heliyon.2024.e24048.

[31] 'Fluent User's Guide'. Accessed: Dec. 01, 2025. [Online]. Available: https://www.afs.enea.it/

[32] J. Ochmann, K. Rusin, M. Jurczyk, S. Rulik, and Ł. Bartela, 'Theory of time constant correlation of a porous bed thermal energy storage tank - Experimental and numerical proof of concept', *Energy*, vol. 308, p. 132956, Nov. 2024, doi: 10.1016/j.energy.2024.132956.

[33] M. M. Kenisarin, 'High-temperature phase change materials for thermal energy storage', *Renewable and Sustainable Energy Reviews*, vol. 14, no. 3, pp. 955–970, Apr. 2010, doi: 10.1016/j.rser.2009.11.011.

[34] K. Vignarooban, X. Xu, A. Arvay, K. Hsu, and A. M. Kannan, 'Heat transfer fluids for concentrating solar power systems – A review', *Applied Energy*, vol. 146, pp. 383–396, May 2015, doi: 10.1016/j.apenergy.2015.01.125.